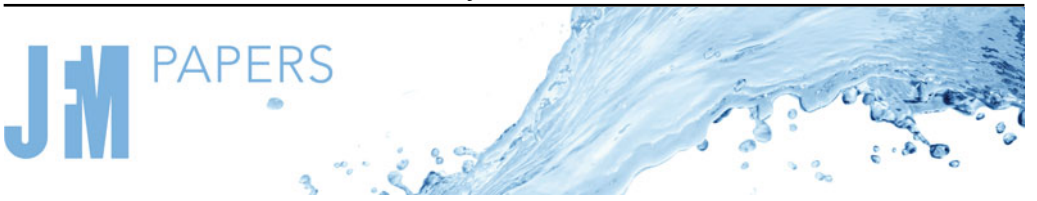
J. Fluid Mech. (2026), *vol.* 1028, A43, doi:10.1017/jfm.2026.11154



The sound-source-oriented coarse-grained Bayesian optimisation for active control of trailing-edge noise

Fu-Yang Yu[1], **Zhen-Hua Wan**[1], **Ya-Sen Hu**[1], **De-Jun Sun**[1] and **Xi-Yun Lu**[1]

[1]State Key Laboratory of High Temperature Gas Dynamics, School of Engineering Science, University of Science and Technology of China, Hefei 230027, PR China

Corresponding authors: Zhen-Hua Wan, wanzh@ustc.edu.cn; Xi-Yun Lu, xlu@ustc.edu.cn

(Received 24 July 2025; revised 7 November 2025; accepted 5 January 2026)

This study implements blowing/suction control for aerofoil trailing-edge noise and systematically optimises blowing/suction angles and control locations within a Bayesian framework. Two distinct rounds were conducted for direct and sound-source-oriented coarse-grained Bayesian optimisations. In the direct optimisation, the mean overall sound pressure level of far-field noise is selected as the objective function. Optimal control parameters were obtained after 15 iterations, requiring 80 three-dimensional implicit large eddy simulations, and achieved a noise reduction of up to 3.7 dB. To reduce the substantial computational cost, a Gaussian process surrogate model was constructed using the sound source defined by multi-process acoustic theory. This enabled a second round of optimisation, termed sound-source-oriented coarse-grained Bayesian optimisation, which yielded comparable noise reduction. This refined approach exhibited low signal delay and rapid statistical convergence, which can significantly reduce both the computational cost per sampling and the iteration number. Consequently, the total computational cost was reduced to approximately one-sixth of the initial direct optimisation. Moreover, physical insights into noise reduction mechanisms were elucidated through dynamic mode decomposition (DMD), anisotropic invariant mapping and the analysis of source terms within the TNO model across several typical cases. The results indicate that the blowing-control case induces large-scale vortex shedding and enhances DMD mode energy and low-frequency noise emission. Furthermore, the suction control tends to disrupt coherent structures, reduce DMD mode energy and suppress radiated noise. Crucially, the suction control significantly decreases mean velocity gradients within the logarithmic layer and suppresses wall-normal Reynolds stresses, thereby considerably reducing TNO source intensity in this critical region. The optimal case exhibits superior performance across all metrics above, thus laying the foundation for the optimal control strategy. Additionally, the suction control facilitates attenuating the footprint of turbulent

© The Author(s), 2026. Published by Cambridge University Press.

https://doi.org/10.1017/jfm.2026.11154 Published online by Cambridge University Press

motions in wall-pressure fluctuations through pressure-velocity coherence analysis, hence promoting noise reduction. This work introduces a novel framework that integrates Bayesian optimisation with advanced noise diagnostic theory, and provides actionable insights for effective trailing-edge noise mitigation.

Key words: aeroacoustics, noise control

1. Introduction

In recent years the rapid development of commercial aviation has elevated flow-induced noise to a prominent environmental concern, with considerable implications for the residential quality of life. The sources of aviation noise are manifold, among which turbulent boundary layer trailing-edge (TBL-TE) noise constitutes an important component of aerofoil self-noise. The TBL-TE noise exhibits distinct broadband characteristics, leading researchers to investigate a range of control strategies (Lee *et al.* 2021; Doolan & Moreau 2022). These noise control methods can be categorised into two groups based on the necessity of external energy input: passive control and active control. Passive control has attracted considerable academic interest due to its operational simplicity and cost effectiveness. Typical passive approaches include trailing-edge serrations (Jones & Sandberg 2012; Chong & Vathylakis 2015; Lyu, Azarpeyvand & Sinayoko 2016; Huang 2017; Avallone *et al.* 2018; Ayton 2018; Pereira *et al.* 2022), porous media (Jaworski & Peake 2013; Kisil & Ayton 2018; Carpio *et al.* 2019; Teruna *et al.* 2020), finlets (Clark *et al.* 2017; Gstrein, Zang & Azarpeyvand 2023; Pan & Ye 2025) and biomimetic coatings (Zhou, Zhong & Zhang 2021). In contrast, active TBL-TE noise control research remains in its early stages (Szőke *et al.* 2020*a*). The advantages of the active method lie in its capacity to achieve flexible and efficient flow and noise control through minimal energy input.

Among active control approaches, blowing/suction has attracted increasing attention for its effectiveness in promoting aerodynamic performance. The early work of Park & Choi (1999) showed that uniform blowing elevates the streamwise vortices and reduces the skin friction in the vicinity of the control slot. However, the skin friction downstream of the blowing slot increases due to enhanced vortices. Kametani & Fukagata (2011), Kametani *et al.* (2015) designed a distributed active control strategy within the turbulent boundary layer. According to their findings, uniform blowing substantially reduces the skin friction drag and intensifies turbulent fluctuations, whereas uniform suction has the opposite effect. Kametani & Fukagata (2011), based on the FIK identity (Fukagata, Iwamoto & Kasagi 2002), demonstrated that the mean convection term plays a critical role in drag reduction, as revealed through the decomposition of the skin friction coefficient. Mahfoze *et al.* (2019) further optimised the intensity and spatial extent of the blowing. Additionally, some studies (Antonia, Zhu & Sokolov 1995; Oyewola, Djenidi & Antonia 2003) indicated that, under moderate momentum thickness Reynolds numbers ($Re_\theta < 660$), sufficiently strong suction can relaminarise the boundary layer. In such cases, the skin friction coefficient is markedly reduced. Some recent studies on aerofoils also confirm the potential of active control techniques (Zha *et al.* 2019; Xu & Zha 2020; Fahland *et al.* 2021; Kornilov, Kavun & Popkov 2021; Quadrio *et al.* 2022).

In the past decade, substantial efforts have been made to leverage blowing/suction techniques for trailing-edge noise mitigation. Although no direct measurements of far-field noise were conducted, the results of the flat plate experiments (Wolf *et al.* 2015; Szőke *et al.* 2020*a*) showed that suction provides significant benefits in reducing trailing-edge

https://doi.org/10.1017/jfm.2026.11154 Published online by Cambridge University Press

noise. Specifically, Wolf *et al.* (2015) reported that flow suction reduces velocity gradients and vertical velocity fluctuations within the boundary layer. The experiments of Szőke *et al.* (2020*a*) further showed that the decrease in the logarithmic layer extent and turbulent energy is responsible for the decrease in mid-frequency surface pressure fluctuations, while the increase in buffer layer energy leads to an increase in high-frequency pressure spectra. Their findings also suggest that there exists an optimal suction angle. Numerical simulations by Cesar, Kamliya Jawahar & Azarpeyvand (2018) demonstrated that suction applied upstream of a NACA0012 aerofoil trailing edge reduces turbulent kinetic energy in the boundary layer and wake, thereby attenuating far-field noise. Moreover, previous findings (Cesar *et al.* 2018; Szőke *et al.* 2020*a*) also demonstrated that the greater the suction intensity, the more pronounced the resulting noise attenuation. Currently, it remains challenging to achieve optimal control effects with a limited suction intensity. Blowing control has also emerged as a promising strategy for noise reduction. Szőke *et al.* (2018) designed a spanwise spaced, inclined transverse jet array to mitigate trailing-edge noise, and the results showed that the control effectiveness depends on blowing intensity and angle. Szőke *et al.* (2020*b*) further investigated the noise reduction efficacy of uniform blowing applied upstream of a flat plate trailing edge. Their experimental results showed that blowing reduces the energy content within the turbulent boundary layer and pushes the turbulent structures away from the wall, ultimately resulting in a noise reduction in the medium-to-high frequency range. Investigations by Moreau *et al.* (2016), Manegar *et al.* (2019) also demonstrated that appropriate blowing on the aerofoil can effectively reduce low-frequency noise. Additionally, some researchers have attempted to apply blowing at the blunt trailing edge of an aerofoil to emulate the function of a splitter plate. Guo *et al.* (2023) and Yang *et al.* (2023) demonstrated that this control method can stabilise the shear layer and reduce the turbulent kinetic energy near the wake, thereby contributing to noise reduction. Yang *et al.* (2024) further combined blowing with trailing-edge serrations to achieve additional noise attenuation. Arnold *et al.* (2018) applied a combined blowing and suction control to reduce wind turbine blade noise by 3.6 dB. Kumar & Bhumkar (2024) demonstrated that periodic suction–blowing excitation can modify tonal noise in laminar boundary layers. Despite blowing/suction methods exhibiting potential in noise reduction, a comprehensive understanding of their noise reduction performance and underlying physical mechanisms remains incomplete, particularly regarding TBL-TE noise.

In engineering, a primary objective is to maximise control effectiveness while simultaneously minimising energy input. Over the years, numerous optimisation methods have been developed to achieve this objective. Widely used optimisation methods include adjoint optimisation (Schulze & Sesterhenn 2013), resolvent analysis (Liang *et al.* 2024), genetic algorithm (Zigunov, Sellappan & Alvi 2022), reinforcement learning (Li & Zhang 2022), amongst others. Recently, a machine learning approach known as Bayesian optimisation, designed to address expensive black-box function optimisation problems, has garnered considerable attention within the fluid dynamics community (Chaitanya & Vellanki 2021; Han, Huang & Xu 2023; Reumschüssel *et al.* 2024). Bayesian optimisation is a derivative-free method that maintains a surrogate model to predict the probability distribution of the objective function while employing an acquisition function capable of balancing exploration and exploitation for decision making (Shahriari *et al.* 2015). To date, the Bayesian optimisation algorithm has been successfully applied across numerous flow control fields, including drag reduction design (Mahfoze *et al.* 2019; Blanchard *et al.* 2021; Han *et al.* 2023), jet mixing enhancement (Blanchard *et al.* 2021; Li *et al.* 2024; Reumschüssel *et al.* 2024) and transition delay (Pershin *et al.* 2022). However, the application of Bayesian optimisation within the field of aeroacoustics remains comparatively limited. Chaitanya & Vellanki (2021) utilised

https://doi.org/10.1017/jfm.2026.11154 Published online by Cambridge University Press

Bayesian optimisation algorithms to optimise the blade shape for the reduction of aerofoil–turbulence interaction noise. Moreover, Lim *et al.* (2022) conducted multi-objective Bayesian optimisation addressing both aerodynamics and aeroacoustics. It should be noted that, owing to computational cost constraints, the aforementioned aeroacoustic studies employed two-dimensional (2D) Reynolds-averaged Navier–Stokes simulations, which may yield less accurate far-field noise estimations. Although Bayesian optimisation algorithms are already highly efficient, the computational cost associated with conducting high-fidelity simulations – such as large eddy simulations – during each sampling stage remains substantial. This is primarily due to the stringent requirements for numerical simulation accuracy and statistical reliability in far-field noise assessment. Currently, reducing the computational burden of the optimisation process remains a significant challenge. One promising approach to addressing this issue involves controlling sound sources based on the acoustic theory, as it enables the avoidance of direct far-field noise calculations during the optimisation process.

This study aims to reduce aerofoil TBL-TE noise through the application of judicious blowing/suction. A parallel Bayesian optimisation algorithm is used to determine the optimal control positions and blowing/suction angles. For each sampling, three-dimensional (3D) large eddy simulations and an acoustic analogy are performed to compute far-field noise. Furthermore, the present study also proposes a sound-source-oriented coarse-grained Bayesian optimisation framework based on multi-process acoustic theory (Mao *et al.* 2020; Hu *et al.* 2022; Yu *et al.* 2025) to reduce computational costs associated with the optimisation process. In addition, the noise reduction mechanisms of the optimal control scenario are investigated through an analysis of modifications in flow structures and noise sources, thereby enhancing the understanding of active flow control techniques.

The remainder of this study is organised as follows. Section 2 provides an introduction to the numerical methods and acoustic theories. The geometry configuration, mesh, simulation details and validations are detailed in § 3. Section 4 presents the optimisation results and the corresponding noise reduction effect. Changes in flow structures and noise suppression mechanisms are also studied by comparing different cases. Finally, § 5 summarises the main findings and provides the conclusion.

2. Numerical methods and acoustic theories

2.1. *The governing equations*

The flow past a NACA0012 aerofoil with or without trailing-edge blowing or suction is solved based on the fully compressible Navier–Stokes equations, which can be non-dimensionalised by the aerofoil chord length l_c, free-stream density ρ_0 and speed of sound c_0. The non-dimensional governing equations are expressed as

$$\frac{\partial \rho}{\partial t} + \frac{\partial}{\partial x_j}(\rho u_j) = 0, \tag{2.1}$$

$$\frac{\partial}{\partial t}(\rho u_i) + \frac{\partial}{\partial x_j}(\rho u_i u_j) = -\frac{\partial p}{\partial x_i} + \frac{\partial}{\partial x_j}(\tau_{ij}), \tag{2.2}$$

$$\frac{\partial}{\partial t}(\rho E) + \frac{\partial}{\partial x_j}(\rho u_j E) = -\frac{\partial}{\partial x_j}(p u_j) + \frac{\partial}{\partial x_j}(\tau_{ij} u_i) - \frac{\partial q_j}{\partial x_j}, \tag{2.3}$$

https://doi.org/10.1017/jfm.2026.11154 Published online by Cambridge University Press

where $E = p/[\rho(\gamma - 1)] + u_j u_j/2$ represents the total energy, p denotes the pressure, ρ is the density and u_i are the velocity components. The viscous stress τ_{ij} and the heat flux term q_j are treated as

$$\tau_{ij} = \frac{\mu Ma}{Re}\left(\frac{\partial u_i}{\partial x_j} + \frac{\partial u_j}{\partial x_i} - \frac{2}{3}\frac{\partial u_m}{\partial x_m}\delta_{ij}\right), \tag{2.4}$$

$$q_j = -\frac{\mu Ma}{(\gamma - 1)PrRe}\frac{\partial T}{\partial x_j}, \tag{2.5}$$

where the Prandtl number Pr and the ratio of gas-specific heat γ are taken as 0.72 and 1.4, respectively. Here $Re = \rho U_0 l_c/\mu_0$ represents the Reynolds number, Ma denotes the Mach number and T is the temperature. The non-dimensional dynamic viscosity coefficient μ is simplified to a constant 1 at the low free-stream velocity, and the equation of state for an ideal gas $p = \rho T/\gamma$ is used to close the equations. In the sponge zone shown in figure 1, we add an artificial damping term to the right-hand side of each governing equation to suppress spurious acoustic reflections, i.e.

$$D_q = -A(r)(\boldsymbol{q} - \boldsymbol{q}_0), \tag{2.6}$$

$$A(r) = B\left\{1 + \mathrm{e}^{\left(\frac{1}{t-1} + \frac{1}{t}\right)}\right\}^{-1}, \tag{2.7}$$

where $t = (r - r_s)/(r_e - r_s)$; r_s and r_e denote the starting and ending locations of the sponge zone, respectively. The maximum damping strength B is taken as 0.05. Here $\boldsymbol{q}$ and $\boldsymbol{q}_0$ are conservation variables and far-field reference quantities. The implicit large eddy simulations (ILES) were conducted based on the open-source solver PyFR (Witherden, Farrington & Vincent 2014), using a third-order flux reconstruction for spatial discretisation. The third-order total variation diminishing Runge–Kutta scheme is used for time advancement. Additionally, all the simulations are conducted on the central processing unit (CPU)/deep computing unit (DCU) parallel heterogeneous platform.

2.2. *The Ffowcs–Williams Hawkings acoustic analogy*

In this study, the far-field noise is predicted by solving the Ffowcs–Williams Hawkings (FW–H) acoustic analogy equation. The convective form of the FW–H equation is employed (Najafi-Yazdi, Brès & Mongeau 2011), i.e.

$$\begin{aligned}&\left[\frac{\partial^2}{\partial t^2} - c_0^2\frac{\partial^2}{\partial x_i \partial x_j} + 2U_{0j}\frac{\partial^2}{\partial t \partial x_j} + U_{0i}U_{0j}\frac{\partial^2}{\partial x_i \partial x_j}\right]\left[H(f)\rho'\right] = \\ &\left(\frac{\partial}{\partial t} + U_{0j}\frac{\partial}{\partial x_j}\right)\left[Q_k n_k \delta(f)\right] - \frac{\partial}{\partial x_i}\left[L_{ij} n_j \delta(f)\right] + \frac{\partial}{\partial x_i \partial x_j}\left[H(f)T_{ij}\right],\end{aligned} \tag{2.8}$$

and

$$\left.\begin{aligned}Q_j &= \left[\rho(u_j' + U_{0j} - v_j) + \rho_0(v_j - U_{0j})\right], \\ L_{ij} &= \left[\rho u_i'(u_j' + U_{0j} - v_j) + (p - p_0)\delta_{ij} - \tau_{ij}\right], \\ T_{ij} &= \rho u_i' u_j' + \left[(p - p_0) - c_0^2(\rho - \rho_0)\right]\delta_{ij} - \tau_{ij},\end{aligned}\right\} \tag{2.9}$$

where Q_j and L_{ij} are the source terms for thickness and loading noise, respectively; T_{ij} denotes the quadrupole noise and can be ignored at a low Mach number; H and δ are the Heaviside function and Dirac function, respectively; U_{0j} is the free stream velocity; f is

https://doi.org/10.1017/jfm.2026.11154 Published online by Cambridge University Press

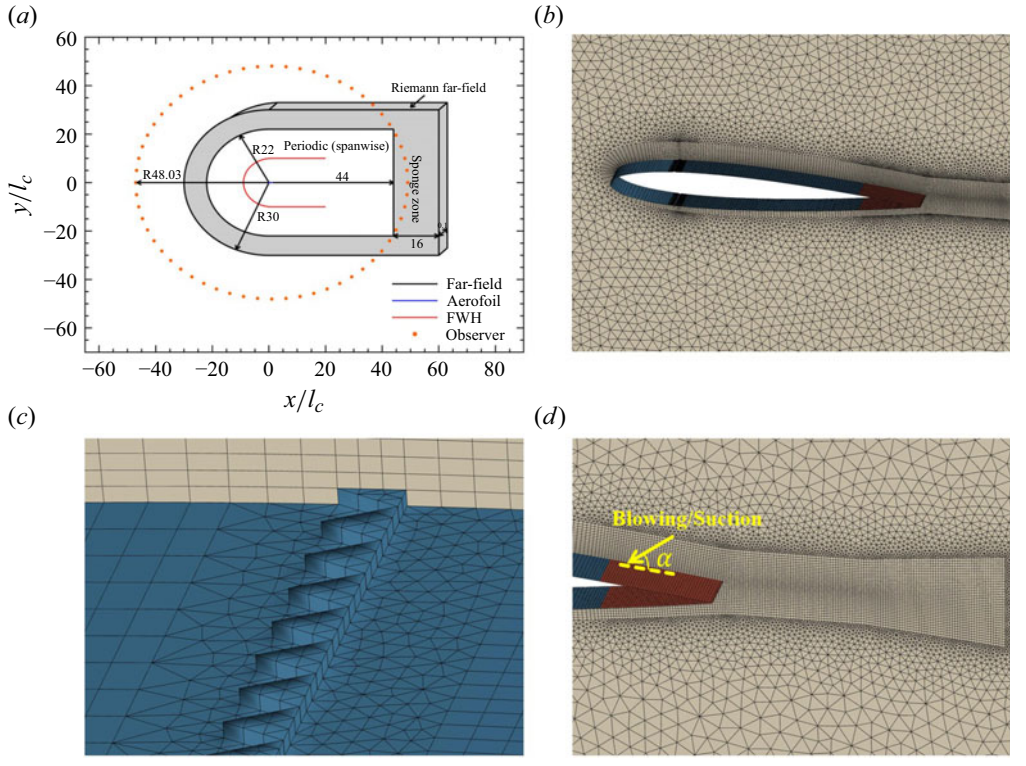


Figure 1. Sketch of the computational zone and the mesh topology: (*a*) the computational zone, including the sponge zone, FW–H integrated face and the far-field observers, (*b*) the global view of the mesh topology, (*c*) the enlarged view near the zig–zag strip, and (*d*) the enlarged view near the trailing edge of the NACA0012 aerofoil.

the penetrable surface, n_i is the unit normal vector of the integration face and $(\bullet')$ denotes fluctuation components. The Green's function is used to solve the FW–H equation, with the physical quantities on the integration surface obtained by ILES. The FW–H integration surface is generated by extruding a single profile along the spanwise direction. This profile consists of a semicircle, located $10l_c$ from the trailing edge, and two attached straight lines with a length of $20l_c$. The position of the FW–H integration surface is shown by the red line in figure 1.

Due to computational cost limitations, the spanwise length in the simulation is shorter than that in the experiment; thus, Herr & Reichenberger (2011) correction is performed and compared with the experimental data, expressed as

$$SPL_{1/3(norm)} = SPL_{1/3} - 50\log(Ma) - 10\log\left(\delta l_z/R_s^2\right), \tag{2.10}$$

where δ is the characteristic outer length scale, l_z is the spanwise length and R_s is the distance from the observer and noise source.

2.3. *The multi-process acoustic theory*

The FW–H equation is capable of accurately predicting far-field noise; however, establishing a direct correlation between the nominal source terms in the FW–H equation and practical noise reduction remains challenging. The multi-process acoustic theory recently developed by Mao *et al.* (2020) obtains a sound mode equation by decomposing the flow into vector transverse and scalar longitudinal processes. The sound mode equation

https://doi.org/10.1017/jfm.2026.11154 Published online by Cambridge University Press

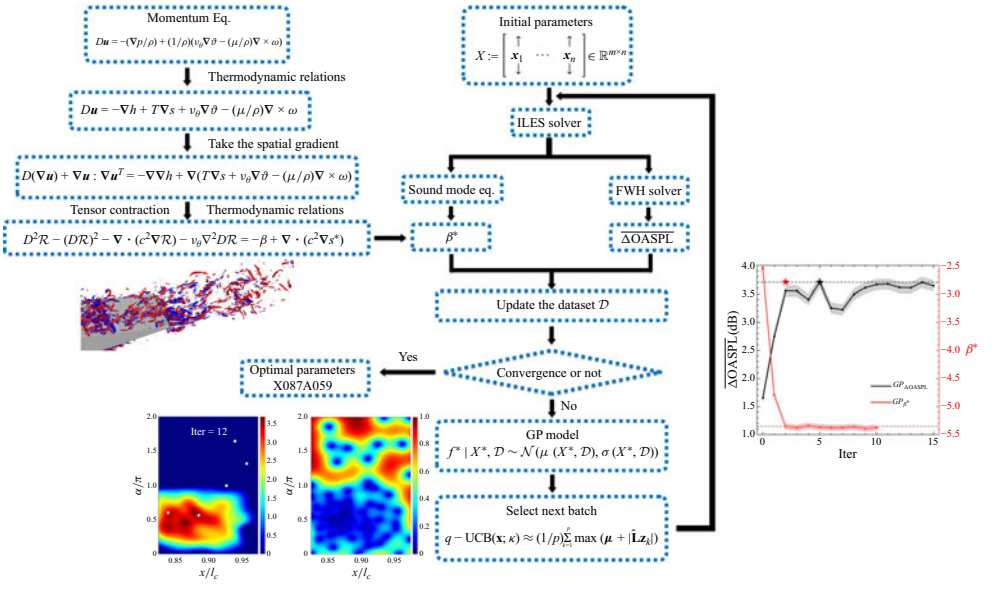


Figure 2. A Bayesian optimisation framework based on the physical acoustic sources and FWH acoustic analogy.

characterises the flow noise sources based on the objective causality in the dynamic equations related to the longitudinal process, with its inhomogeneous convective form expressed as

$$D^2\mathcal{R} - (D\mathcal{R})^2 - \boldsymbol{\nabla}\cdot\left(c^2\boldsymbol{\nabla}\mathcal{R}\right) - \nu_\theta\nabla^2 D\mathcal{R} = -\beta + \boldsymbol{\nabla}\cdot\left(c^2\boldsymbol{\nabla}s^*\right), \tag{2.11}$$

where $\mathcal{R} = \ln(\rho/\rho_0)$ is the dimensionless acoustic variable, $s^* = (s - s_0)/c_p$ is the relative entropy change, c_p is the specific heat at constant pressure, D denotes the material derivative, $\nu_\theta = (\lambda + 2\mu)/\rho$ represents the longitudinal kinematic viscosity and λ stands for the bulk viscosity. Here, $\beta = (\vartheta\boldsymbol{I} - \boldsymbol{\nabla}\boldsymbol{u}^T) : \boldsymbol{\nabla}\boldsymbol{u}$ is considered as a pseudo 'inviscid work rate' done by the nonlinear inertial force over the boundary of the unit mass control volume; ϑ and $\boldsymbol{I}$ are the dilatation and the second-order unit tensor, respectively. At low-Mach-number conditions, the entropy term $\boldsymbol{\nabla}\cdot(c^2\boldsymbol{\nabla}s^*)$ can be ignored owing to the limited temperature change, and the shear noise source (β) plays a dominant role. In the multi-process acoustic theory, the source terms have a clear physical interpretation and do not incorporate sound propagation effects. This characteristic facilitates the connection between changes in the physical source and far-field noise reduction. Additionally, the definition of the shear noise source is compact, and its computation can be directly derived from the spatial discretisation of the flow equations, making it advantageous and convenient for noise optimisation. A brief derivation of the sound mode equation is presented in figure 2, where h and $\boldsymbol{\omega}$ denote enthalpy and vorticity, respectively.

2.4. *Bayesian optimisation algorithm*

In the present work, a parallel Bayesian optimisation algorithm (Wilson *et al.* 2017) is employed to optimise blowing or suction control in the vicinity of the aerofoil trailing edge, aiming to achieve the objective of reducing far-field noise. This algorithm can mitigate the risk of falling into local optima while simultaneously reducing the overall optimisation time. There are two major components of the Bayesian optimisation workflow: first, a surrogate model is employed to predict the objective function for unseen data points,

https://doi.org/10.1017/jfm.2026.11154 Published online by Cambridge University Press

and then an appropriate optimisation policy is used to determine the optimal location for the next samples.

Currently, the Gaussian process (GP) is selected as the surrogate model. Its predictions are provided in the form of probability distributions, enabling us to quantify the uncertainty in predictions and thereby better balance risk and reward in decision making. Specifically, suppose that the optimisation parameter space is m-dimensional and the objective function is denoted as $f(\boldsymbol{x})$. Initially, we create n points through a random number generator and compute their objective function values. Thus, the training dataset is $\mathcal{D} := \{X, \boldsymbol{f}\}$, where

$$X := \begin{bmatrix} \uparrow & & \uparrow \\ \boldsymbol{x}_1 & \cdots & \boldsymbol{x}_n \\ \downarrow & & \downarrow \end{bmatrix} \in \mathbb{R}^{m\times n}, \quad \boldsymbol{f} := \begin{bmatrix} f(\boldsymbol{x}_1) \\ \vdots \\ f(\boldsymbol{x}_n) \end{bmatrix} \in \mathbb{R}^n. \tag{2.12}$$

In this study, $m = 2$ and $n = 5$. Subsequently, a GP model is trained on this dataset, enabling

$$f^* \mid X^*, \mathcal{D} \sim \mathcal{N}\left(\mu\left(X^*, \mathcal{D}\right), \sigma\left(X^*, \mathcal{D}\right)\right), \tag{2.13}$$

where X^* is the test input and f^* represents the corresponding predicted values. Here $\mu(X^*, \mathcal{D})$ and $\sigma(X^*, \mathcal{D})$ are the mean and covariance matrix of a multivariate normal distribution, respectively, satisfying

$$\mu\left(X^*, \mathcal{D}\right) = \boldsymbol{K}\left(X^*, X\right)\left(\boldsymbol{K}(X, X) + \sigma_n^2 \boldsymbol{I}\right)^{-1} \boldsymbol{f}, \tag{2.14}$$

$$\sigma\left(X^*, \mathcal{D}\right) = \boldsymbol{K}\left(X^*, X^*\right) - \boldsymbol{K}\left(X^*, X\right)\left(\boldsymbol{K}(X, X) + \sigma_n^2 \boldsymbol{I}\right)^{-1} \boldsymbol{K}\left(X, X^*\right), \tag{2.15}$$

where $\boldsymbol{K}(X, X^*)$ is a kernel matrix capturing the correlations between elements. To improve numerical stability, Gaussian noise $\epsilon \sim \mathcal{N}(0, \sigma_n^2)$ is added into the observations (Jenkins, Gerstoft & Park 2023). The Matérn 5/2 kernel function (Stein 1999; Matérn 2013) is employed in the current study, expressed as

$$\boldsymbol{K}\left(X, X^*\right) = \sigma_f^2 \left(1 + \sqrt{5} d\left(\boldsymbol{x}_i, \boldsymbol{x}_j^*\right) + \frac{5}{3} d^2\left(\boldsymbol{x}_i, \boldsymbol{x}_j^*\right)\right) \exp\left(-\sqrt{5} d\left(\boldsymbol{x}_i, \boldsymbol{x}_j^*\right)\right), \tag{2.16}$$

$$d\left(\boldsymbol{x}_i, \boldsymbol{x}_j^*\right) = \sqrt{\sum_{k=1}^{m} \frac{\left(x_{i,k} - x_{j,k}^*\right)^2}{\ell_k^2}}, \tag{2.17}$$

where σ_f^2 denotes the covariance amplitude and ℓ_k represents the length scale. The hyperparameters in GP are optimised by maximising the marginal likelihood, which automatically trades off the data fit against model complexity and thereby mitigates overfitting.

Following this, a Bayesian optimisation policy takes in the trained GP surrogate to identify the optimal location for the next samples through an acquisition function. Conventional Bayesian optimisation follows a sequential sampling strategy. In contrast, this work implements a parallel upper confidence bound (q-UCB) acquisition function to diminish the optimisation time (Wilson *et al.* 2017). The q-UCB trades off exploitation and exploration. In a q-UCB we need to simultaneously select q points, whose joint posterior distribution follows $\mathcal{N}(\boldsymbol{\mu}, \boldsymbol{\Sigma})$. Here $\boldsymbol{\mu} \in \mathbb{R}^q$ is the mean vector and $\boldsymbol{\Sigma} \in \mathbb{R}^{q\times q}$ is the covariance matrix. Specifically, a q-UCB can be expressed as

https://doi.org/10.1017/jfm.2026.11154 Published online by Cambridge University Press

Parameters	Values	Parameters	Values
Ma	0.1631	Re_c	9.6×10^4
l_z	0.1	ϕ	0°
x_Δ	0.2	h_Δ	0.0025
l_Δ	0.01	λ_Δ	0.0125
dt	8×10^{-5}	DoF	$\approx 3 \times 10^7$
b	0.05	C_μ	0.8

Table 1. The details for flow simulations. Here Ma is the free-stream Mach number, Re_c denotes the Reynolds number based on the aerofoil chord length, l_z is the non-dimensional spanwise length, ϕ is the angle of attack, and x_Δ, h_Δ, l_Δ, and λ_Δ represent the position, height, width and spanwise wavelength of the transition strip, respectively; dt is the dimensionless time step, DoF is the degree of freedom of the mesh and b and C_μ are the streamwise length and intensity of the flow control.

$$q-\mathrm{UCB}(\boldsymbol{x};\kappa)=\int_{-\infty}^{\infty}\max(\boldsymbol{\mu}+|\hat{\boldsymbol{L}}\boldsymbol{z}|)\mathcal{N}(\boldsymbol{z};\boldsymbol{0},\boldsymbol{I})\mathrm{d}\boldsymbol{z}, \tag{2.18}$$

where $\hat{\boldsymbol{L}}\hat{\boldsymbol{L}}^\top=\tilde{\boldsymbol{\Sigma}}=(\kappa\pi/2)\boldsymbol{\Sigma}$. The above integral can be approximated using the Monte Carlo method:

$$q-\mathrm{UCB}(\boldsymbol{x};\kappa)\approx\frac{1}{p}\sum_{k=1}^{p}\max(\boldsymbol{\mu}+|\hat{\boldsymbol{L}}\boldsymbol{z}_k|),\quad \boldsymbol{z}_k\sim\mathcal{N}(\boldsymbol{0},\boldsymbol{I}). \tag{2.19}$$

In the above acquisition function, κ serves as a pivotal hyperparameter. Larger κ values bias the strategy toward exploration of uncertain regions, while smaller κ values favour exploitation of known optima. In this study, $q=5$, $p=512$ and $\kappa=2$. Note that the q-UCB method focuses on the maximum value in a batch of data rather than the average performance of the batch.

Two rounds of Bayesian optimisation were conducted. In the first round, the far-field noise was directly optimised; in the second round, near-field acoustic sources were utilised to construct the GP model. All other optimisation parameters remained unchanged. A schematic diagram of the aforementioned Bayesian optimisation algorithms is presented in figure 2. The iteration can be considered converged when the historical optimum of the objective function falls within the statistical error margin of the best value for five consecutive iterations.

3. The configurations of the numerical model

3.1. *The computational schemes and meshes*

Similar to the numerical simulation conditions conducted by Hu *et al.* (2022), a NACA0012 aerofoil is placed in a uniform flow at $Ma=0.1631$. The zig–zag strips are installed on both sides of the aerofoil to ensure a complete boundary layer transition. The detailed simulation parameters are presented in table 1. A schematic illustration of the computational domain is depicted in figure 1(*a*). The origin of the Cartesian coordinate system is placed at the aerofoil leading edge, with the x axis aligned with the free-stream direction, the y axis normal to the chord and the z axis coinciding with the spanwise direction.

An adiabatic no-slip boundary condition is applied at the solid wall, while the periodic boundary condition is imposed on the spanwise direction. The Riemann condition is specified at the far field, and steady blowing/suction is employed at the control slots.

https://doi.org/10.1017/jfm.2026.11154 Published online by Cambridge University Press

In this study, both the length of the control slot b and the flow control intensity C_μ are held constant at $0.05l_c$ and 0.8, respectively. The definition of flow control intensity is consistent with that of Szőke *et al.* (2020*a*), i.e. $C_\mu = u_c b/u_0\theta_0$, where $u_c \approx 0.09$ and $\theta_0 \approx 0.0056l_c$ denote the blowing/suction velocity and the momentum thickness of the uncontrolled boundary layer near the trailing edge. Notably, in the experiment by Szőke *et al.* (2020*a*), the suction intensity ranged from 1.8 to 9.1. However, the present study aims to achieve optimal control effectiveness with minimal energy consumption, so the flow control intensity is significantly lower than the values used in that experiment. The objective of this work is to achieve maximum noise reduction under low flow control intensity, where the centre position x/l_c and angle of blowing/suction α are defined as parameters to be optimised. The control slot is positioned near the trailing edge, with its centre location x/l_c varying from 0.825 to 0.975 in the chordwise position, corresponding to a potential coverage domain of [0.8, 1.0]. The potential installation region for the control slot is illustrated by the red surface in figure 1(*b*). The active control angle domain spans $[0, 2\pi]$, where angles in $[0, \pi]$ denote suction and those in $[\pi, 2\pi]$ represent blowing. The definition of the blowing/suction angle is illustrated in figure 1(*d*).

All controlled cases are computed by restarting from the solution of the uncontrolled case. The dimensionless time step and sampling time interval are 8×10^{-5} and 1×10^{-2}, respectively. The duration to eliminate the restart transient is $25l_c/U_0$, and the noise statistics are collected for 200 dimensionless times (about 32 flow-past times). The fluctuation signal is partitioned into four segments with 50 % overlap between adjacent sections, and a Hanning window is applied to minimise spectrum leakage.

The same grid is adopted for all cases. The enlarged view of the mesh topology is presented in figure 1(*b–d*). Hexahedral elements are implemented in the near-wall and near-wake regions with a stretching ratio of 1.05, while tetrahedral elements populate the vicinity of the transition strip and far-field domains. The minimum wall distance Δy^+ of the solution point is maintained below 1 to fully resolve the viscous sublayer. The total degree of freedom (DoF) is approximately 3×10^7, distributed along the aerofoil span with 80 solution points.

3.2. *Validation*

For validation purposes, the results of the uncontrolled case are compared against previous numerical (Hu *et al.* 2022) and experimental data (Brooks *et al.* 1989; Lee & Kang 2000). Figure 3 presents the mean pressure coefficient on the wall, the skin friction coefficient in the turbulent boundary layer region and the normalised sound pressure level (SPL) in 1/3-octave bands at the probe of $(x/l_c, y/l_c, z/l_c) = (1.0, 48.03, 0.05)$. The present results show good agreement with previous numerical and experimental data, indicating the reliability of the current study. The sudden change in the pressure coefficient in figure 3(*a*) is due to the transition strip applied in the numerical model. There is a small area of inconsistency between the present results and Hu *et al.* (2022)'s results after the transition trip. This is likely due to the numerical overshoot caused by the transition from tetrahedral to hexahedral elements at approximately $x/l_c \approx 0.25$ in the current study. Since this region is located far from the areas of noise generation and control application, it does not have a fundamental impact on the optimisation results presented in this research. The differences between the numerical and experimental SPL in figure 3(*c*) should result from the difference in turbulence tripping methods and the unresolved small scales. In figure 3(*c*) we also provide the noise prediction results obtained using an integration surface with a closing cap and a computational domain with doubled spanwise extent. It can be observed that selecting different integration surfaces or increasing the spanwise length does not significantly alter the current results.

https://doi.org/10.1017/jfm.2026.11154 Published online by Cambridge University Press

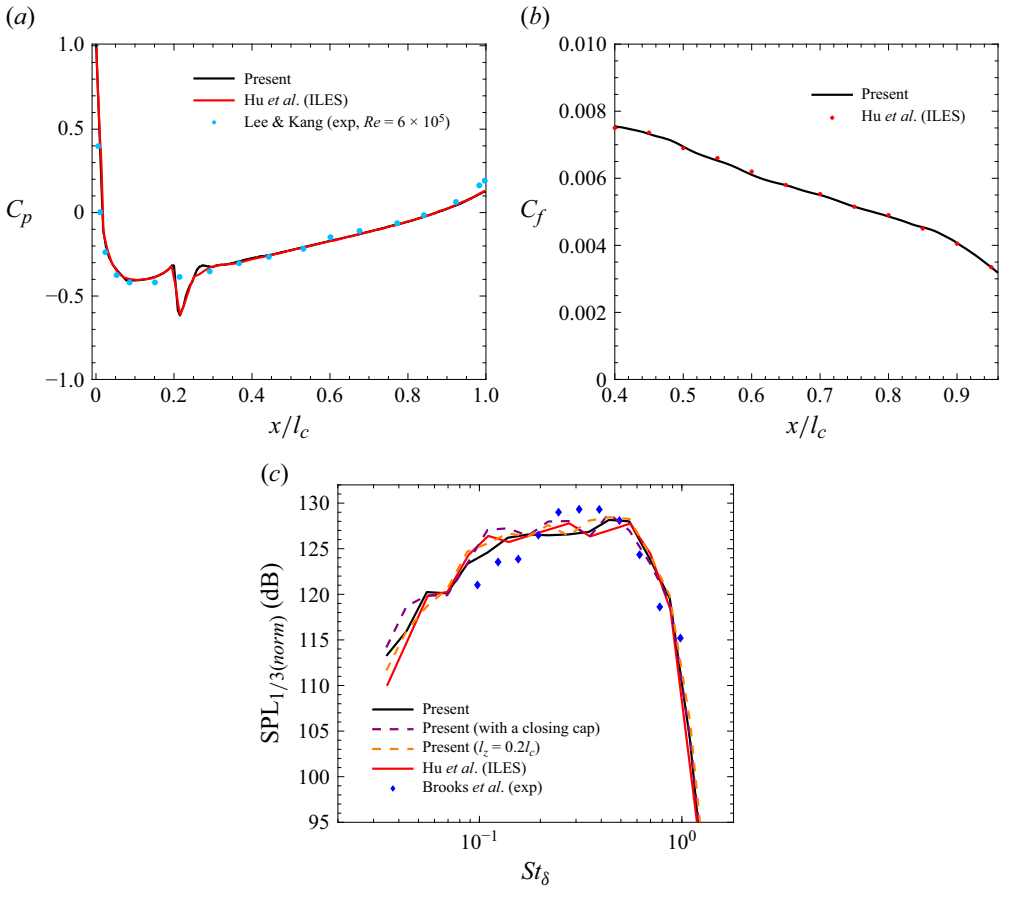


Figure 3. Comparisons between the present ILES data and previous studies (Brooks, Pope & Marcolini 1989; Lee & Kang 2000; Hu *et al.* 2022): (*a*) mean pressure coefficient distribution on the surface of the aerofoil, (*b*) the skin friction coefficient in the turbulent boundary layer region, and (*c*) the normalised sound pressure level (SPL) in 1/3-octave bands. The observer is located at $(x/l_c, y/l_c, z/l_c) = (1.0, 48.03, 0.05)$, and $St_\delta = f\delta_{99}/U_c$ is the Strouhal number based on the boundary layer thickness and convection velocity. The turbulent boundary layer thickness δ_{99}/l_c in the current study, Hu *et al.* (2022)'s numerical simulation and Brooks *et al.* (1989)'s experiment are 0.0426, 0.0426, and 0.0753, respectively.

4. Results and discussion

4.1. *The results of Bayesian optimisation*

Bayesian optimisation is carried out to determine the optimal parameters for active control, specifically the centre position of slot x/l_c and the blowing/suction angle α, for noise reduction. Naturally, the change in the far-field overall SPL (OASPL) is chosen as the metric for assessing noise reduction. In this direct optimisation process the mean overall sound pressure reduction level ($\overline{\Delta\mathrm{OASPL}}$) over the direction range from about 40° to 140° is designated as the objective function. The observers are distributed along a circle as indicated by the orange dots in figure 1(*a*). The angular separation between adjacent monitors is 6°. As shown in figure 4, a GP model is employed to compute the posterior distribution of the objective function, including the mean and uncertainty of the noise reduction level. The subsequent sampling location is determined via the q-UCB acquisition policy. Here, the uncertainty in the data is quantified by the variance

https://doi.org/10.1017/jfm.2026.11154 Published online by Cambridge University Press

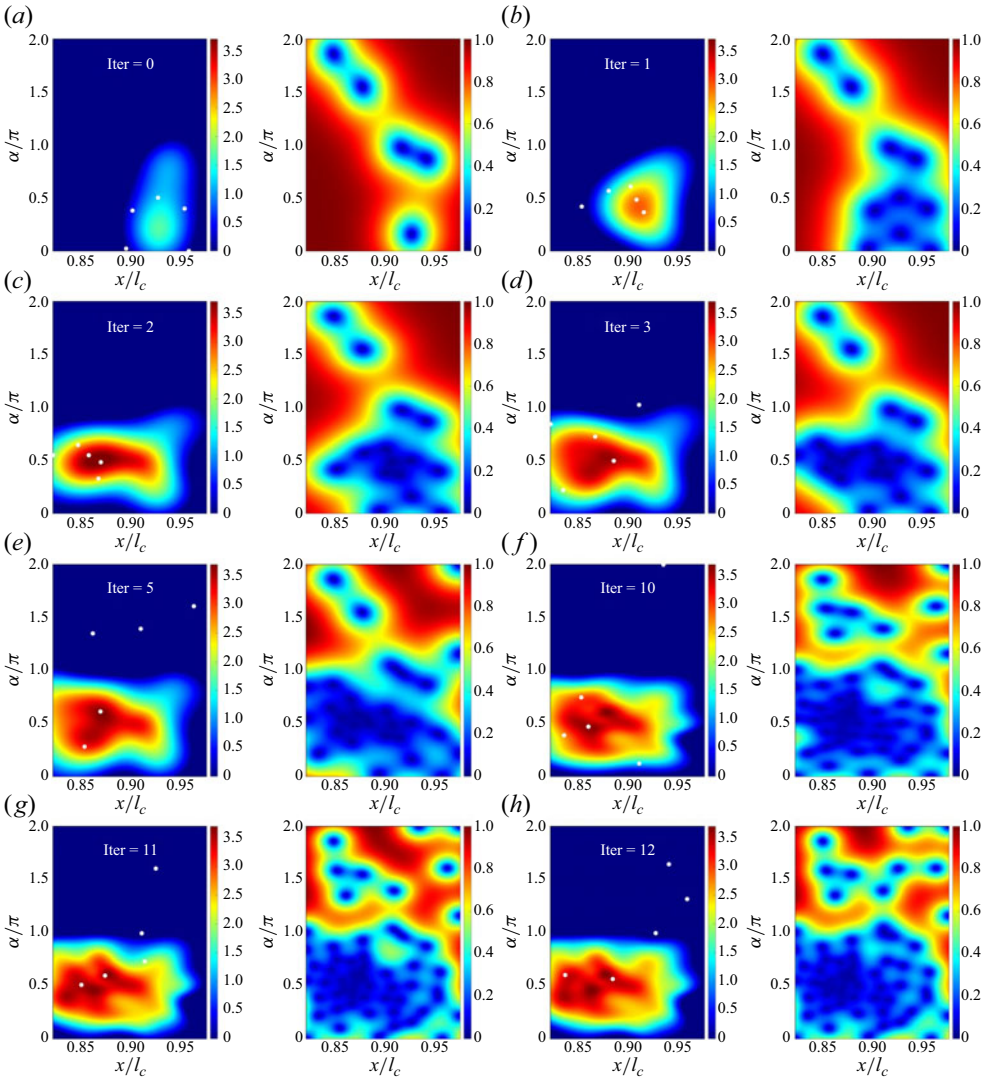


Figure 4. Progress made by the Bayesian optimisation. The GP predictions at (*a*) iteration 0, (*b*) iteration 1, (*c*) iteration 2, (*d*) iteration 3, (*e*) iteration 5, (*f*) iteration 10, (*g*) iteration 11 and (*h*) iteration 12 are displayed. In each subplot, the left and right panels display the $\overline{\Delta\mathrm{OASPL}}$ values and the uncertainty of the data predicted by the 2D GP model, respectively.

predicted by the surrogate model and normalised by the maximum variance across all prediction points. Thus, in the right panel of each subgraph, a value of 1 represents a high level of prediction uncertainty, while a value of 0 indicates that the prediction is already quite accurate. The uncertainty drops sharply to zero at the sampling locations, resulting in distinct minima in the visualisation. In the left panel of each subgraph, all regions predicted to have increased noise are displayed in blue. Additionally, we use white points to indicate the location for the next sampling batch guided by the q-UCB strategy. In this study, one iteration step updates five sampling points simultaneously.

Figure 4 shows the prediction results of some iteration steps in the first direct Bayesian optimisation process in detail. As shown in figure 4(*a*), we generated the initial dataset using random numbers. The sampling point locations are in the blue parts of the right

https://doi.org/10.1017/jfm.2026.11154 Published online by Cambridge University Press

panel. The GP model generated from the initial dataset in the left panel identifies a promising region within the parameter space near the sampling point at the bottom-right corner, where noise reduction is anticipated. Subsequent sampling locations are strategically concentrated around this region. Following the first iteration, as depicted in figure 4(*b*), the noise reduction region is updated, with the predicted next sampling location shifting leftward (toward the trailing edge upstream). By the second iteration, both the predicted noise reduction region and the next sampling location further move upstream. Meanwhile, a data point demonstrating over 3.5 dB noise reduction has emerged in the current dataset. After three iterations, the predicted noise reduction trend has taken initial shape. In the fifth iteration (figure 4*e*) we identify the optimal parameters for this round of optimisation. The optimal control parameters include a position located at $x/l_c = 0.8734$ and an angle of 0.5895π, which can achieve a noise reduction of up to 3.7 dB. In the experiments on parametric suction control at high Reynolds numbers ($Re = 10^6$) by Szőke *et al.* (2020*a*), the optimal suction angle was 0.61π (note that the angle definition in the experiment differs from that in this paper), which is very close to the optimal parameter of 0.5895π in this study. Note that optimal control incurs a certain drag penalty, increasing the drag coefficient by about 22 %. This implies a conflict between noise reduction effectiveness and aerodynamic performance. After 10 iterations, as illustrated in figure 4(*f–h*), the GP model begins predicting multiple local maxima in noise reduction while the global maximum remains unchanged. At this stage, the q-UCB acquisition strategy exhibits a distinctive behavioural pattern: within each batch of sampling points, one or two consistently localise near existing extrema while others probe unexplored regions of the parameter space. This indicates that the q-UCB scheme balances exploration and exploitation while avoiding getting trapped in local optima. After sufficient iterations, the uncertainty value corresponding to the noise reduction region has become relatively small. Therefore, we can consider that the predictions provided by the GP model are tending towards accuracy. The black solid line in figure 5 further shows the history of the objective function for our first Bayesian optimisation. Considering a statistical error of ± 0.1 dB, we can regard the current iteration as having converged, with the optimal value found at the fifth iteration.

The final GP model is built from a total of 80 high-fidelity samples and is displayed in figure 6(*a*). The ultimate surrogate model exhibits several noteworthy findings. Under the current simulation set-up, all blowing controls produce the result of noise enhancement, corresponding to the region where $\alpha/\pi > 1$ in figure 6(*a*). Notably, suction controls positioned close to the trailing edge fail to yield effective control outcomes. However, when we shift the suction slot upstream, normal suction demonstrates improved performance. As the suction slot continues to move further upstream, the effective range of suction angles gradually expands. Nevertheless, when the suction slot is positioned significantly away from the trailing edge, the efficacy of suction control slightly diminishes. Moreover, the GP model in figure 6(*a*) exhibits multiple local extrema, with the optimal control parameters identified through our iterative process marked by black pentagrams.

It should be emphasised that although Bayesian optimisation efficiently identifies optimal control parameters, its computational cost remains prohibitively high for 3D aeroacoustic applications. Acoustic simulations typically demand high fidelity, extended statistical sampling duration and incur computational overhead from far-field signal delays, collectively making each sampling iteration prohibitively expensive. Taking the aforementioned optimisation procedure as an example, it consumed approximately 1×10^5 DCU-hours in total by utilising 20 DCU cards over a period of more than seven months. Consequently, we attempt to integrate multi-process acoustic theory into the

https://doi.org/10.1017/jfm.2026.11154 Published online by Cambridge University Press

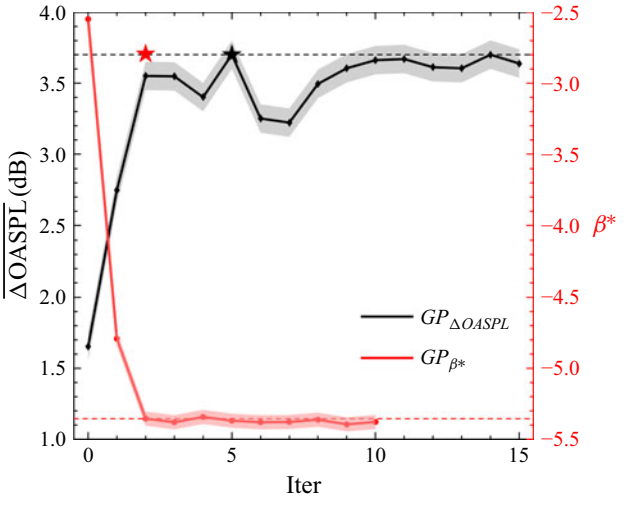


Figure 5. The optimisation history of the $\overline{\Delta\mathrm{OASPL}}$ (solid black line) and β^* (solid red line). The black shaded area indicates the error range of ± 0.1 dB and the red shaded area represents the error range of ± 0.05. The black pentagram marks the optimum noise reduction value based on GP models constructed by $\overline{\Delta\mathrm{OASPL}}$, and the red pentagram indicates the maximum noise reduction corresponding to GP models constructed by β^*.

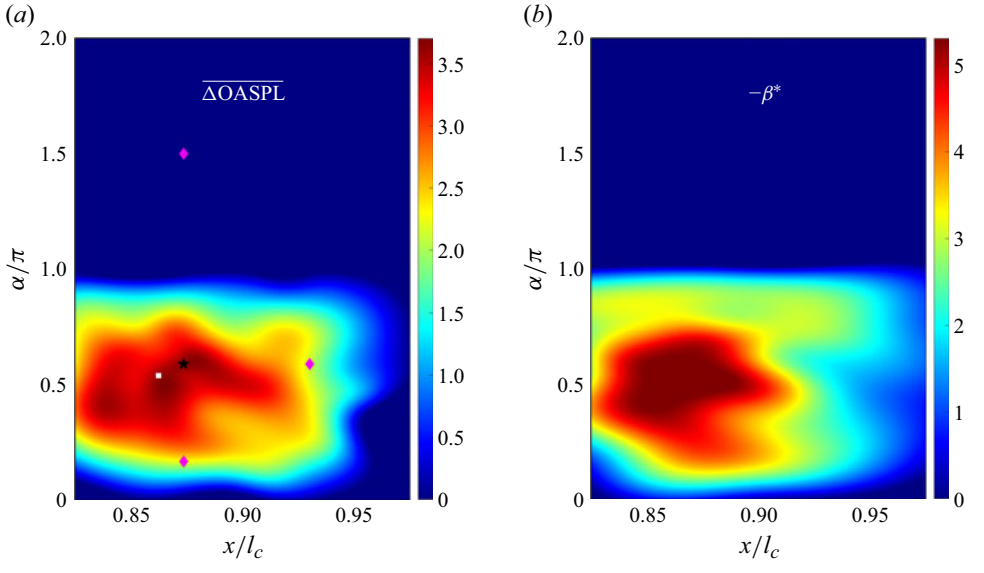


Figure 6. Comparison of GP models based on (*a*) far-field noise reduction $\overline{\Delta\mathrm{OASPL}}$, and (*b*) near-field physical noise source strength $-\beta^*$. Both GP models utilise the same full set of 80 sample points from the first round of Bayesian optimisation. The black pentagram represents the optimal noise reduction point, while magenta diamonds denote points used for comparison in subsequent analysis. The white square denotes the optimal parameters identified during the second iteration of the source-oriented Bayesian optimisation.

Bayesian optimisation framework to circumvent direct far-field noise computation, thereby achieving significant computational savings. In this study we define a near-field noise source strength β^* defined in the multi-process acoustic equation (Mao *et al.* 2020),

https://doi.org/10.1017/jfm.2026.11154 Published online by Cambridge University Press

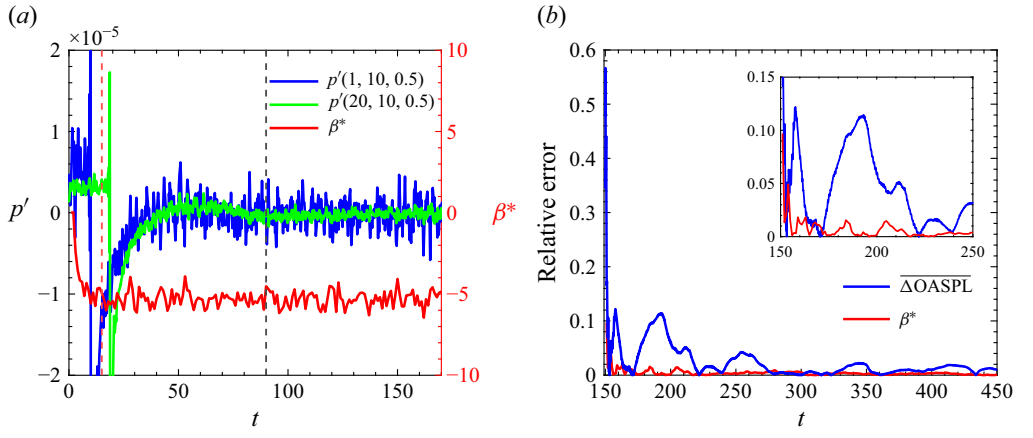


Figure 7. Comparison of costs between statistical far-field noise reduction and near-field physical noise sources for the optimal case: (*a*) the signal delay of pressure fluctuations on the FWH face and near-field physical noise source strength, and (*b*) the statistical convergence of $\overline{\Delta\mathrm{OASPL}}$ and β^*.

formulated analogously to the overall SPL. Here β^* is given by

$$\beta^* = 10\log_{10}\left(\frac{\int \overline{\beta^2}\mathrm{d}V}{\int \overline{\beta_0^2}\mathrm{d}V}\right), \tag{4.1}$$

where β and β_0 denote the shear noise source with and without control, respectively. Here $(\bar{\bullet})$ represents the time average; V denotes the domain for physical source integration, selected to encompass main trailing-edge noise scattering regions and also include partial wake structures, i.e. $V \in [l_c - 2\delta_0, l_c + \delta_0] \times [-1.5\delta_0, 1.5\delta_0] \times [0, 0.1l_c]$ (δ_0 is the boundary layer thickness for the uncontrolled case). A positive value of $-\beta^*$ indicates a decrease in sound source intensity, whereas a negative value signifies an increase.

Before the second round of Bayesian optimisation, we first examine whether the GP model constructed from the near-field physical source intensity can capture the trend of noise reduction. In figure 6(*b*) the dataset for the surrogate model comprises all 80 ILES results obtained by the previous optimisation process. Notably, the parameter space with increased source intensity is shaded blue. Comparing the far-field noise reduction GP model (i.e. figure 6*a*) with the physical source intensity GP model (figure 6*b*) reveals some interesting phenomena. First, all blowing-control cases exhibit increased noise source intensity. Second, suction slots adjacent to the trailing edge show less significant source intensity reduction. As the control slot shifts upstream, normal suction initially demonstrates favourable sound source attenuation, followed by an expansion of the effective suction angle range. Finally, the regions exhibiting significant attenuation of sound source intensity broadly coincide with those achieving substantial noise reduction. All the above findings align consistently with the trends observed in far-field noise variation. It should also be mentioned that the GP model of β^* exhibits inadequate resolution in regions where $\overline{\Delta\mathrm{OASPL}} > 3.3$ dB, failing to resolve multiple local extremes in figure 6(*a*). In general, the selection of β^* for constructing the surrogate model should have effectively captured the dominant physical mechanisms, which is crucial for its application in coarse-grained optimisation.

It is worth emphasising that selecting β^* as the objective function offers additional advantages. Figure 7(*a*) compares the time delay between far-field pressure fluctuations and near-field noise sources. The blue pressure signal is recorded at the FW–H surface

https://doi.org/10.1017/jfm.2026.11154 Published online by Cambridge University Press

directly above the trailing edge, while the green pressure signal is measured at a position further downstream. Here, $t = 0$ denotes the moment when control is activated, i.e. the restart moment. It can be seen that the far-field monitors detect the effects of control after a long time delay: the blue signal responds at $t \approx 10$ (1.6 flow-past times) and the green signal at $t \approx 20$ (3.3 flow-past times). Moreover, the requisite waiting period for signal stabilisation on the FW–H surface is considerably longer, necessitating at least 90 non-dimensional time units (14.7 flow-past times) before initiating noise statistics. In contrast, β^* responds to the control almost instantaneously ($t \approx 0$), enabling us to start a statistical analysis of sound source intensity as early as $t \approx 15$ (2.4 flow-past times). Figure 7(*b*) further compares the statistical convergence of $\overline{\Delta\mathrm{OASPL}}$ and β^*, where the relative error is defined as

$$\text{Relative error} = \left| \frac{q_t - q_{ref}}{q_{ref}} \right|, \tag{4.2}$$

where q denotes $\overline{\Delta\mathrm{OASPL}}$ or β^*. We consider the value obtained from sufficiently long-duration statistics ($t = [150, 550]$, approximately 65 flow-past times) as the reference value q_{ref}. Here q_t represents the value accumulated up to time t, where $t = 150$ is the moment when the statistics start. Evidently, β^* converges more rapidly than $\overline{\Delta\mathrm{OASPL}}$. The current noise statistics satisfy an error tolerance below 0.1 dB, corresponding to a relative error <0.027. Attaining improved statistical convergence would necessitate a substantially extended sampling duration. In contrast, achieving a noise source intensity statistical error below 0.1 (relative error <0.02) requires less than 10 non-dimensional times. Additionally, the computation of shear sound sources imposes no additional computational overhead on ILES, as these values can be obtained directly from the spatial discretisation of the governing equations. In short, the combination of robust physical representation, reduced signal latency and faster statistical convergence enables Bayesian optimisation based on physical noise sources to substantially reduce computational costs.

Next, we examine the effects of the sound-source-oriented coarse-grained Bayesian optimisation. During the coarse-grained optimisation process, β^* is selected to construct the GP model, with the initial dataset consistent with the first round of optimisation. In this optimisation, 75 dimensionless time units are used to eliminate transient effects, followed by an additional 75 units for source statistics. All other settings remain identical to the first optimisation round. Under the current statistical approach, the single sampling cost of source-oriented Bayesian optimisation is approximately 40 % of that for direct Bayesian optimisation. However, this statistical estimation is highly conservative. If we adopt a less conservative statistical method, i.e. initiating measurement immediately upon signal stabilisation while maintaining identical statistical error thresholds (0.1 dB for $\overline{\Delta\mathrm{OASPL}}$ and 0.1 for β^*), the single sampling cost of coarse-grained optimisation would thus be reduced to approximately 10 %. The history of this optimisation is shown as a red solid line in figure 5. Within the margin of statistical error, parameters minimising source strength were identified as early as the second iteration. Additionally, we calculate the maximum noise reduction for samples in the second iteration step (statistical analysis over 200 dimensionless time units), as indicated by the red pentagram. Notably, the use of physical source intensity enables faster identification of optimal parameters. Under the current statistical strategy, the comprehensive cost has been reduced to about one-sixth of the original. The cost calculation here is based on a reduction in per-sample cost to 40 %, with the number of iterations required to find the optimum or achieve convergence also reduced to 40 % of the original, without accounting for the cost of generating the initial dataset. It should be noted that while different initial datasets can influence the

https://doi.org/10.1017/jfm.2026.11154 Published online by Cambridge University Press

Cases	C_μ	x/l_c	α/π
Baseline	0	—	—
X087A059	0.8	0.8734	0.5895
X087A017	0.8	0.8734	0.1667
X093A059	0.8	0.9300	0.5895
X087A150	0.8	0.8734	1.5000

Table 2. The cases used for noise and flow structure analysis. The uncontrolled case is selected as the baseline case.

iterative process, using a physical source is likely to converge faster due to the smoother surrogate model of β^*, as shown in figure 6(*b*). Additionally, the white square in figure 6(*a*) shows optimal parameters from the second iteration in the source-oriented optimisation. As illustrated, the coarse-grained optimisation identifies an alternative extremum from the perspective of sources. The control effect approaches the global optimum achieved through direct Bayesian optimisation, while the control parameters remain close to their counterparts in the first round of optimisation. The discrepancy between the optimal parameters obtained from coarse-grained optimisation and the global optimum should be mainly attributed to the measurement method of the source term, including the selected spatial region and the defined objective function of the source term. Overall, the source-oriented method demonstrates the effectiveness of the optimisation process and can be directly deployed for noise control applications. Additionally, it can also be used to rapidly constrain the search domain to facilitate locating the global optimum.

4.2. *Noise emission and flow structures*

In this section we focus on discussing the changes in far-field noise and near-field flow structures induced by blowing and suction control. To this end, we have selected the uncontrolled case for comparison with the optimally controlled case (X087A059). Furthermore, two additional cases are included: one featuring a different suction angle (X087A017) and another with a different suction location (X093A059). Additionally, one blowing case (X087A150) exhibiting a noise intensification effect is selected as a reference to facilitate a more comprehensive examination of the source mechanism. These points used for analysis are indicated by the markers in figure 6(*b*), with the detailed parameter settings given in table 2.

Figure 8 illustrates the distribution of far-field pressure fluctuations across different frequency bands, normalised by the maximum value along the circle for the uncontrolled case depicted in figure 8(*a*). Subsequently, we define the low-frequency band as $St = [2, 6]$, the mid-frequency band as $St = [6, 14]$ and the high-frequency band as $St = [14, 20]$. For the blowing case, different ticks are used for the whole-frequency band and low-frequency band, as labelled by the magenta ticks. It can be observed from profiles of $\sqrt{\langle p'^2 \rangle}$ that suction control has no significant effect on altering the noise propagation direction across different frequency bands. In contrast, blowing control alters the primary radiation direction of low-frequency noise, thereby influencing the overall radiation pattern across the entire frequency band. Specifically, the dominant acoustic propagation direction is about 132° for both the uncontrolled and suction cases in figure 8(*a*), whereas it shifts to about 114° for the blowing case. At low frequencies, all suction control cases achieve significant reductions in far-field pressure fluctuations. Two dominant lobes are observed, suggesting the presence of compact dipole sources near the trailing edge. Among these, the optimal case X087A059 exhibits the most effective low-frequency noise reduction

https://doi.org/10.1017/jfm.2026.11154 Published online by Cambridge University Press

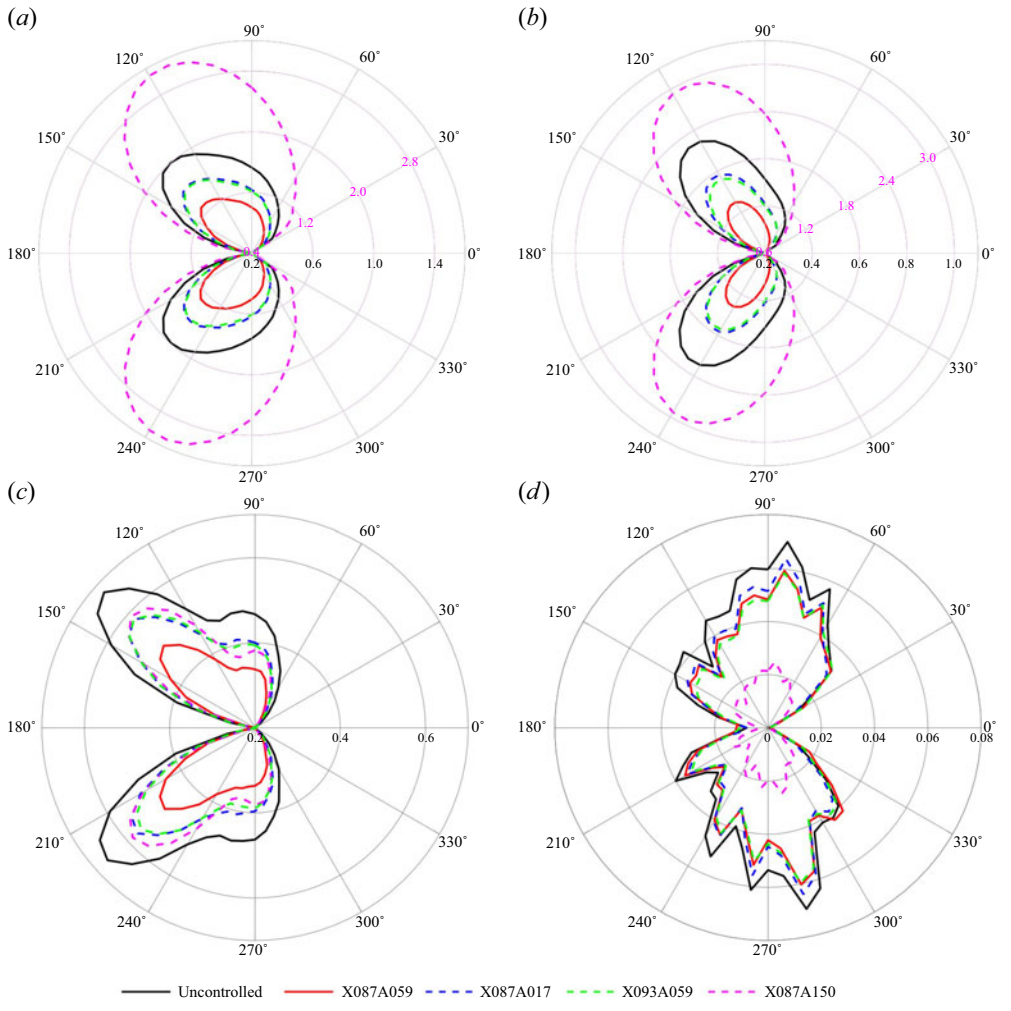


Figure 8. Directivity plot of the acoustic intensity $\sqrt{\langle p'^2 \rangle}$ on a circle with radius $R = 48.03 l_c$ in various frequency ranges, with the Strouhal number defined as $St = f l_c / U_0$: (*a*) whole-frequency band, $St = [0, 20]$, (*b*) low-frequency band, $St = [2, 6)$, (*c*) mid-frequency band, $St = [6, 14)$, and (*d*) high-frequency band, $St = [14, 20]$.

capability. Conversely, the blowing-control case X087A150 substantially increases the amplitude of low-frequency pressure fluctuations. In the mid-frequency range, all cases achieve a certain degree of noise reduction. Similarly, case X087A059 demonstrates the best control performance. Additionally, some non-impact properties occur accompanied by four lobes pointing to $\theta \approx \pm 138°$ and $\theta \approx \pm 90°$. At high frequencies, the distribution of far-field pressure fluctuations becomes increasingly irregular. Among the selected cases, the blowing case X087A150 demonstrates the most effective control performance, while the noise reduction capabilities of the suction cases remain relatively similar.

Figure 9 displays the acoustic propagation patterns and instantaneous vortex structures for the selected cases. From the dilatation field, it can be seen that the sound waves are generated by scattering at the aerofoil trailing edge. Suction control attenuates acoustic wave intensity, whereas blowing significantly amplifies SPLs with a pronounced increase in long-wavelength components. The isosurfaces of Q in figure 9(*d*) demonstrate that

https://doi.org/10.1017/jfm.2026.11154 Published online by Cambridge University Press

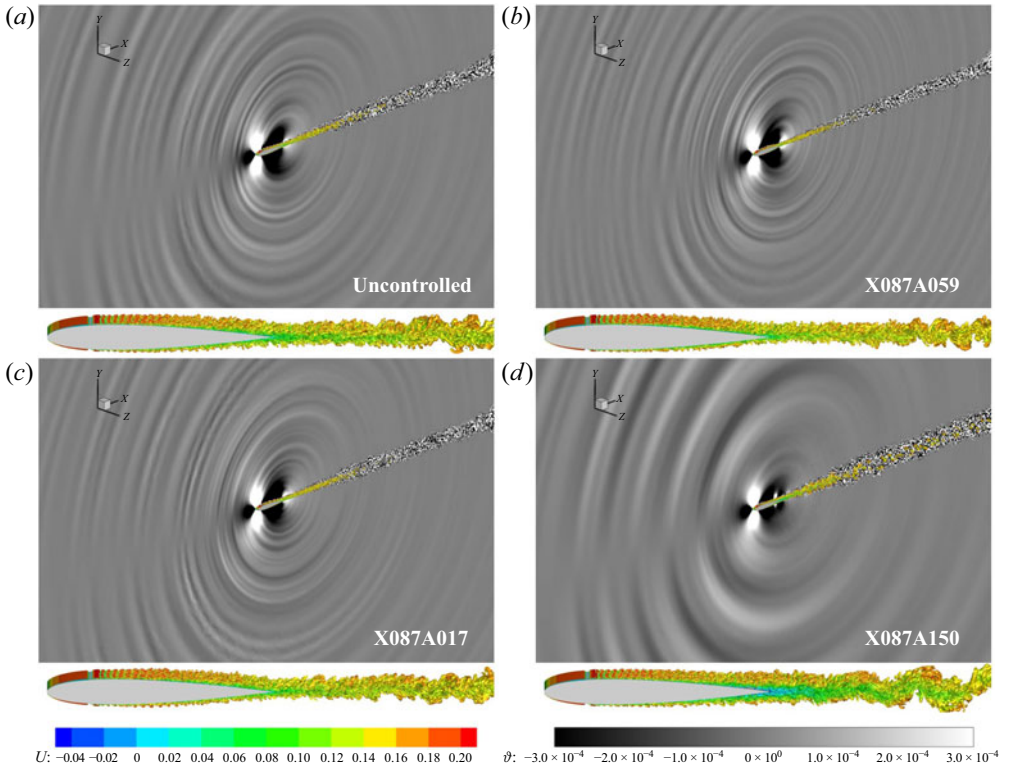


Figure 9. Instantaneous sound propagation and vortex structures shown by the dilatation ϑ and isocontours of the Q-criterion ($Q = 0.1$ coloured by streamwise velocity): (*a*) the uncontrolled case, (*b*) the optimal case X087A059, (*c*) the suction case X087A017, and (*d*) the blowing case X087A150.

blowing induces additional large-scale vortex shedding in the wake, thereby triggering low-frequency noise enhancement. In contrast, suction control primarily narrows the core separation of wake vortices without substantially altering the flow pattern. This observation aligns with the unchanged noise radiation directivity of the suction cases in figure 8.

Dynamic mode decomposition (DMD) (Schmid 2010) is further employed to clarify the effects of blowing and suction controls on flow structures. A sequence of continuous pressure fluctuation field snapshots is assembled into matrices $\boldsymbol{P}_1^{N-1}$ and $\boldsymbol{P}_2^{N}$, i.e.

$$\boldsymbol{P}_1^{N-1} = \boldsymbol{P}_{\boldsymbol{x},t(1\ldots N-1)} = \begin{bmatrix} p'(\boldsymbol{x}_1,t_1) & p'(\boldsymbol{x}_1,t_2) & \ldots & p'(\boldsymbol{x}_1,t_{N-1}) \\ p'(\boldsymbol{x}_2,t_1) & p'(\boldsymbol{x}_2,t_2) & \ldots & p'(\boldsymbol{x}_2,t_{N-1}) \\ \vdots & \vdots & \ddots & \vdots \\ p'(\boldsymbol{x}_i,t_1) & p'(\boldsymbol{x}_i,t_2) & \ldots & p'(\boldsymbol{x}_i,t_{N-1}) \end{bmatrix}, \tag{4.3}$$

$$\boldsymbol{P}_2^{N} = \boldsymbol{P}_{\boldsymbol{x},t(2\ldots N)} = \begin{bmatrix} p'(\boldsymbol{x}_1,t_2) & p'(\boldsymbol{x}_1,t_3) & \ldots & p'(\boldsymbol{x}_1,t_N) \\ p'(\boldsymbol{x}_2,t_2) & p'(\boldsymbol{x}_2,t_3) & \ldots & p'(\boldsymbol{x}_2,t_N) \\ \vdots & \vdots & \ddots & \vdots \\ p'(\boldsymbol{x}_i,t_2) & p'(\boldsymbol{x}_i,t_3) & \ldots & p'(\boldsymbol{x}_i,t_N) \end{bmatrix}, \tag{4.4}$$

https://doi.org/10.1017/jfm.2026.11154 Published online by Cambridge University Press

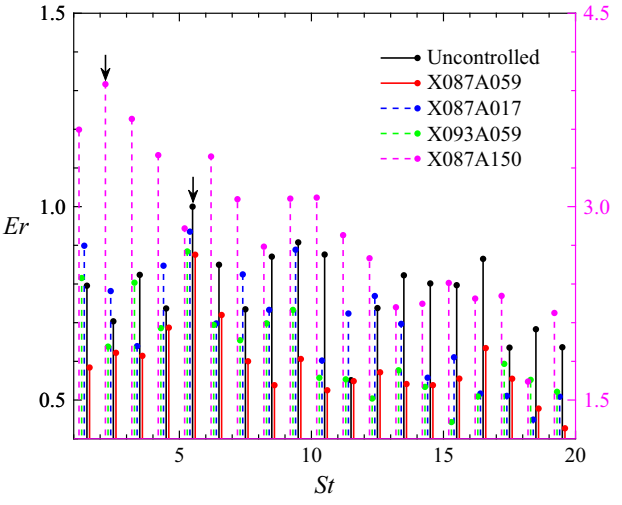


Figure 10. Distribution of DMD mode energy ratios across various frequency bands. Here, the left black y ticks on the left are adopted for the baseline and suction cases, and the magenta y ticks on the right are used for the blowing case X087A150.

where $\boldsymbol{P}_1^{N-1}$ and $\boldsymbol{P}_2^N$ represent the matrices corresponding to time steps 1 to $N-1$ and 2 to N, respectively. The time interval is taken as $\Delta t = 0.1 l_c/c_0$ and the number of snapshots is 500. $\boldsymbol{x}$ contains all solution points excluding the sponge zone. Assume that there exists a linear mapping operator $\boldsymbol{A}$ describing the dynamic characteristics of the flow system, that is,

$$\boldsymbol{P}_2^N = \boldsymbol{A}\boldsymbol{P}_1^{N-1} = \boldsymbol{P}_1^{N-1}\boldsymbol{S} + \boldsymbol{r}\boldsymbol{e}_{N-1}^T, \tag{4.5}$$

where $\boldsymbol{S}$ is the adjoint operator, $\boldsymbol{r}$ denotes the residual and $\boldsymbol{e}_{N-1}^T$ represents the $(N-1)$th vector of the identity matrix. The eigen-decomposition of the adjoint operator $\boldsymbol{S}$ can be expressed as

$$\boldsymbol{S}\boldsymbol{q} = \lambda \boldsymbol{q}. \tag{4.6}$$

The eigenvalue λ and eigenvector $\boldsymbol{q}$ can be obtained via the singular value decomposition. The DMD modes are denoted by $\boldsymbol{\phi}_i = \boldsymbol{L}\boldsymbol{q}_i$, with the corresponding mode frequencies being $St = \mathrm{Im}(\log(\lambda)) l_c/(2\pi U_0 \Delta t)$. Here, $\boldsymbol{L}$ represents the left singular matrix and Im denotes the imaginary part operator. The energy of the pressure mode denoted E_{ϕ_i} is defined as the L_2-norm of the modal vector. For comparison purposes, the energy ratio is defined as

$$Er_j = \sum_{St_{\phi_i} \in [j-1, j]} E_{\phi_i}/E_0, \quad j = 1, 2, 3, \ldots, 20, \tag{4.7}$$

where E_0 is the sum of mode energies in the most energetic frequency band ($St = [5, 6]$) for the uncontrolled case. Figure 10 presents the distribution of mode energy ratios across different frequency bands for various cases. Note that the blowing case X087A150 employs distinct tick marks. For the uncontrolled case, and all suction cases, i.e. X087A059, X087A017 and X093A059, the $St = [5, 6]$ band constitutes the most energetic frequency range, which is correlated with hydrodynamically unstable waves exhibiting the most pronounced convective amplification. Assuming a convection velocity of $U_c = 0.7U_0$, the corresponding characteristic spatial scale $\lambda_{ch} = U_c/f$ for this band ranges

https://doi.org/10.1017/jfm.2026.11154 Published online by Cambridge University Press

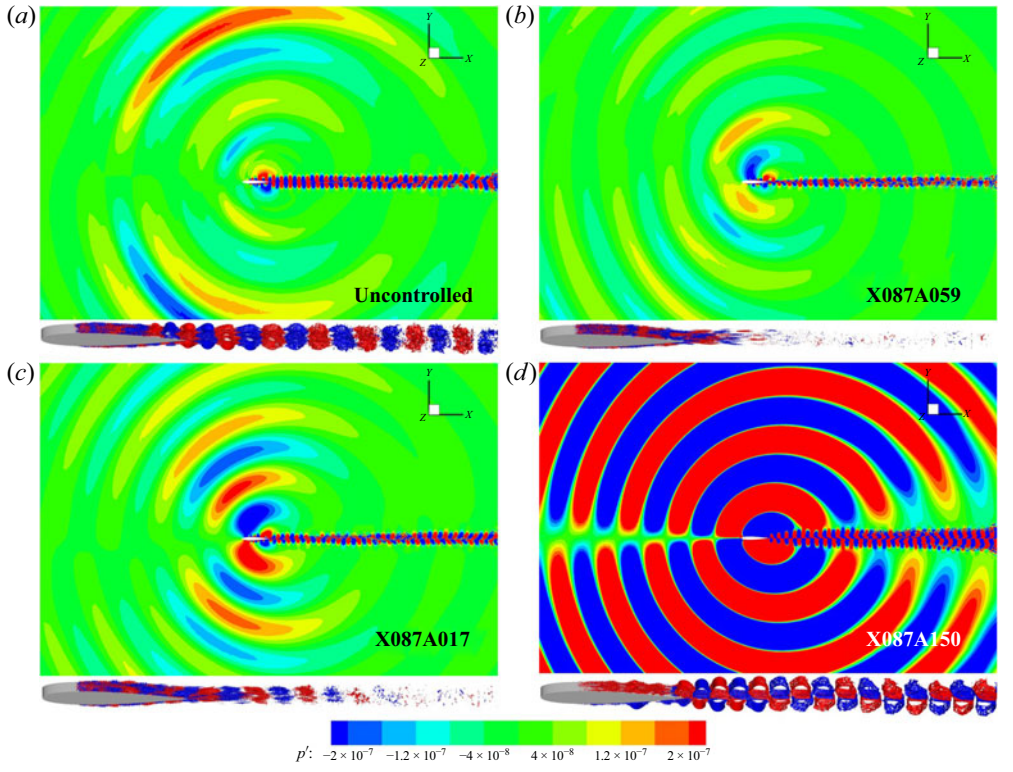


Figure 11. The slice view ($z = 0.05l_c$) of the real part of the most energetic pressure mode at $St \approx 2.5$ for various cases and the corresponding isocontours of the mode structures: (*a*) the uncontrolled case, (*b*) the optimal case X087A059, (*c*) the suction case X087A017, and (*d*) the blowing case X087A150.

from $0.117l_c$ to $0.140l_c$. In contrast, the most energetic frequency for case X087A150 occurs at $St \approx 2.85$. Here, the dominant frequency band ($St = [2, 3]$) is associated with blowing-induced large-scale vortex shedding. The wavelength of these large-scale vortices is estimated as $\lambda_{vs} = U_c l_c/(2.85U_0) \approx 0.25l_c$, aligning with both the measured shedding wavelength in figure 9(*d*) and the mode structure wavelength in figure 11(*d*). Furthermore, compared with the uncontrolled case, blowing elevates the overall mode energy, while suction effectively attenuates mode energy across most frequency bands. Notably, the optimal control case X087A059 demonstrates the superior performance, achieving a significant reduction in mode energy throughout all frequency bands. Next, the analysis is conducted for modes with the most energy at two typical frequencies, i.e. $St \approx 2.5$ and $St \approx 5.5$, as indicated by black arrows in figure 10.

Figure 11 presents the DMD modes corresponding to the frequency $St \approx 2.5$. It can be observed that the baseline case exhibits regular near-field flow structures. The suction control can disrupt this regular pattern. In the optimal control case X087A059, the flow structure in the wake has become barely discernible in figure 11(*b*). The near-field structures in the less effective suction case X087A017 still exhibit weaker wake structures in figure 11(*c*). However, the blowing cases exhibit an entirely distinct flow mode – specifically, antisymmetric mode structures associated with large-scale vortex shedding. The radiated pressure fluctuations also correlate with changes in the near-field mode patterns. Among these, case X087A059 exhibits the weakest radiated noise, followed by the less effective suction case X087A017, while the blowing case X087A150 shows

https://doi.org/10.1017/jfm.2026.11154 Published online by Cambridge University Press

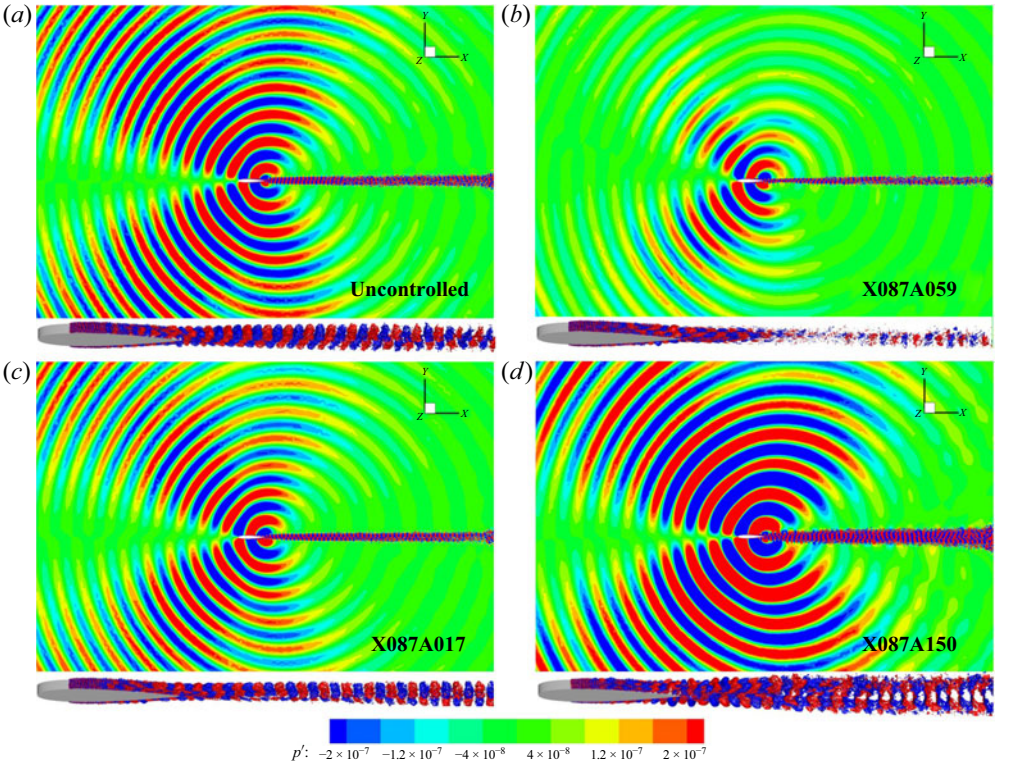


Figure 12. The slice view ($z = 0.05l_c$) of the real part of the most energetic pressure mode at $St \approx 5.5$ for various cases and the corresponding isocontours of the mode structures: (*a*) the uncontrolled case, (*b*) the optimal case X087A059, (*c*) the suction case X087A017, and (*d*) the blowing case X087A150.

significantly enhanced noise radiation. Figure 12 displays the most energetic mode around the frequency $St \approx 5.5$. Similar to the low-frequency mode, the radiated noise decreases in the suction cases, while it increases in the blowing cases. The control effect is most effective in the optimal case X087A059. At current mode frequencies, the dominant radiation directions are pointing toward the upstream. The near-field flow structure also undergoes significant changes. Compared with the mode at $St \approx 2.5$, the flow structures in figure 12 exhibit shorter wavelengths. Both suction control and blowing control induce structural distortion in the wake. Specifically, the optimal suction control (X087A059) causes rapid dissipation of flow structures, whereas the blowing control (X087A150) results in stronger wake structures that persist for longer distances.

To quantitatively characterise variations in turbulent structures across different regions of the trailing-edge boundary layer, the anisotropy invariant map method is employed (Pope 2001; Simonsen & Krogstad 2005). In the case of negligible compressibility, the anisotropic part of the Reynolds stress tensor is expressed as follows:

$$b_{ij} = \frac{\langle u_i' u_j' \rangle}{\langle u_k' u_k' \rangle} - \frac{1}{3}\delta_{ij}. \tag{4.8}$$

The second and third principal invariants I_2 and I_3 can be determined through the roots of the corresponding characteristic polynomial, namely,

https://doi.org/10.1017/jfm.2026.11154 Published online by Cambridge University Press

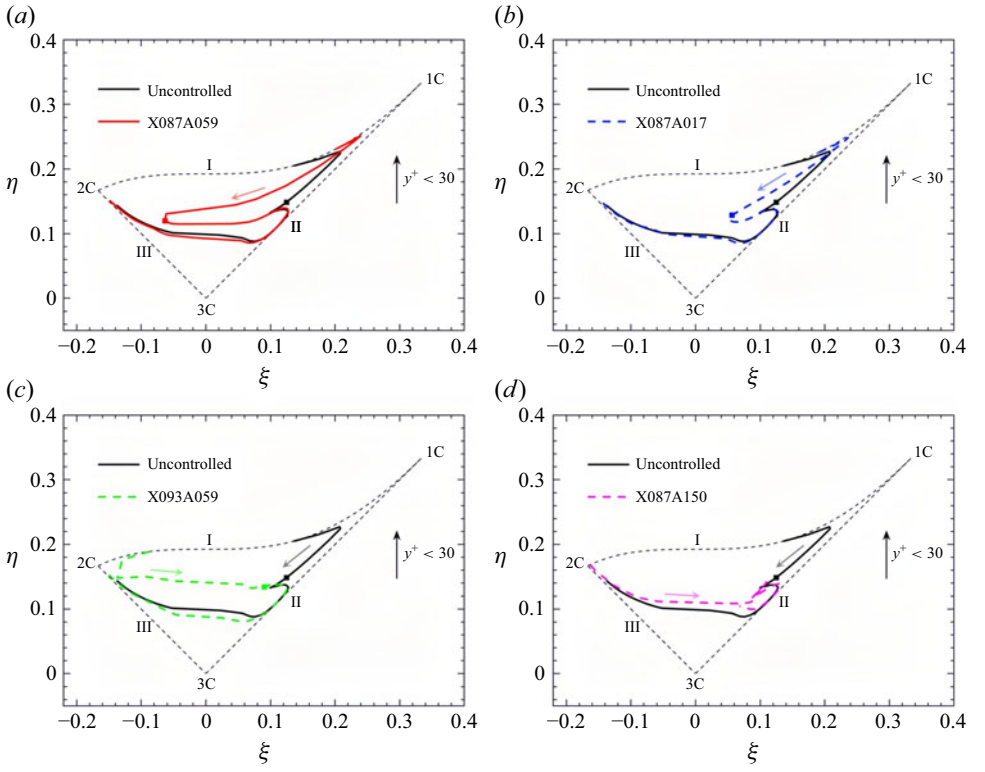


Figure 13. Anisotropy invariant map with different wall-normal distances at $x = 0.96l_c$. The two-component turbulence, rod-like axisymmetric turbulence and disk-like axisymmetric turbulence regimes are demarcated by black dashed lines I, II, and III, respectively. Here 1C, 2C, and 3C denote single-component turbulence, two-component axisymmetric turbulence and isotropic turbulence, respectively. The square symbols in the figure represent the location at $y^+ \approx 30$, while the upper portion of the curves corresponds to smaller y^+ values.

$$I_2 = -\frac{1}{2} b_{ij} b_{ji}, \qquad I_3 = \det([b_{ij}]). \tag{4.9}$$

Lumley & Newman (1977) argued that these invariants provide a complete description of turbulence anisotropy characteristics. To gain immediate visual insight, we select two independent invariants for turbulent stress invariance analysis, defined as follows (Pope 2001):

$$6\eta^2 = -2I_2 = b_{ij} b_{ji}, \qquad 2\xi^3 = I_3 = \det([b_{ij}]). \tag{4.10}$$

Figure 13 displays the anisotropy invariant map with different wall-normal distances at $x = 0.96l_c$, where turbulence regimes delimited by black dashed boundaries are annotated in the legend. Active flow control is shown to modify near-wall turbulence structures at the trailing edge significantly. As can be seen from figure 13(*a–b*), the viscous sublayer ($y^+ \lesssim 5$) corresponds to the region leftward of the upper-right inflection point in the anisotropy invariant map for the uncontrolled case and the two upstream suction cases (X087A059, X087A017). Flow states within this domain align more closely with the two-component turbulence regime defined by curve I. Notably, the inflection points for cases X087A059 and X087A017 shift toward the single-component turbulence limit.

https://doi.org/10.1017/jfm.2026.11154 Published online by Cambridge University Press

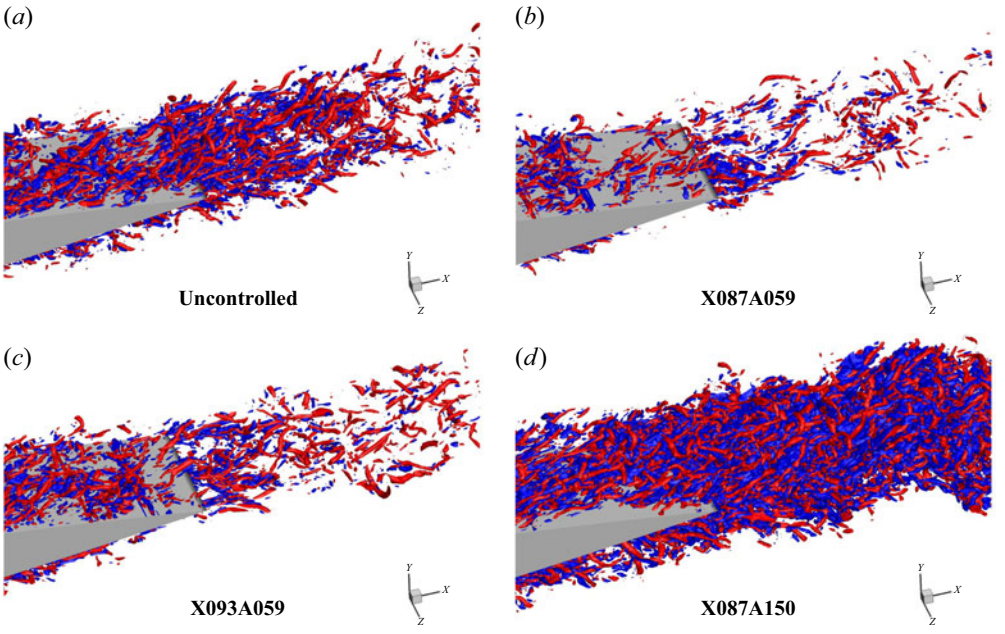


Figure 14. Isocontours of the instantaneous physical noise source structures for (*a*) the uncontrolled case, (*b*) the optimal case X087A059, (*c*) the suction case X093A059, and (*d*) the blowing case X087A150. The isosurfaces of $-\beta = \pm 100$ (blue colour for $-\beta = 100$ and red colour for $-\beta = -100$) are displayed near the trailing edges.

In the buffer layer ($5 \lesssim y^+ \lesssim 30$), turbulence in the uncontrolled case approaches a rod-like axisymmetric state. Case X087A017 shows a slight deviation from this state, while the optimal control case (X087A059) exhibits a more significant departure. In figure 13(*c*), suction control near the trailing edge (X093A059) exhibits distinct behaviour: Its near-wall region ($y^+ \lesssim 30$) shows flow structures evolving toward disk-like turbulence (curve III). In the logarithmic layer, turbulence states for the suction cases gradually revert to uncontrolled conditions (see figure 13*a–c*). Among these, the optimal suction case (X087A059) maintains noticeable modifications within the logarithmic layer. At higher boundary layer positions, turbulence shifts from rod-like (curve II) toward disk-like (curve III) states. Here, differences between uncontrolled and suction cases become less noticeable. For the blowing case (X087A150 in figure 13*d*), $y^+ \approx 30$ values have not been provided due to the presence of near-wall reverse flow. Here, disk-like turbulent structures appear near the wall, while rod-like structures emerge farther from the wall. In summary, blowing control induces distinct anisotropy patterns across the entire boundary layer, whereas suction control primarily affects the near-wall region. Among suction cases, the optimal X087A059 demonstrates the most significant alterations in the logarithmic layer.

Considering that the multi-process acoustic theory (Mao *et al.* 2020) offers a robust method for quantifying changes in noise source structures, figure 14 illustrates the spatial distribution of instantaneous shear acoustic sources near the trailing edge across various cases. In the uncontrolled case, the acoustic source structure is predominantly concentrated near the trailing edge. Suction significantly diminishes this structure, while the optimal case (X087A059) exhibits a markedly weakened acoustic source structure compared with case X093A059. Conversely, blowing (X087A150) substantially amplifies the acoustic source structure, extending it into the wake.

https://doi.org/10.1017/jfm.2026.11154 Published online by Cambridge University Press

In summary, blowing control induces additional vortex shedding, significantly altering the flow structure and markedly increasing the acoustic source intensity, which drives the observed rise in low-frequency noise. Conversely, suction control tends to disrupt the flow structure near the wall, reducing the acoustic source intensity. The mechanisms behind this reduction and the noise suppression in the optimal suction control case (X087A059) require further investigation. The noise reduction mechanism for optimal control will be explored in the next subsection.

4.3. *Noise reduction mechanisms*

As evidenced in the above subsection, suction control modifies turbulent structures in the near field. These modifications to the flow structures inevitably affect the wall-pressure fluctuations near the trailing edge, leading to a reduction in far-field noise. Here, pressure–velocity coherence analysis is employed to understand the effect of turbulent motion on wall-pressure fluctuations (Pan & Ye 2025). The pressure–velocity coherence definition proposed by Zang, Mayer & Azarpeyvand (2020) is utilised to eliminate spurious coherence regions, expressed as

$$C_{p'u_i'}(St,\, y^+) = \frac{\left|\phi_{p'u_i'}(St,\, y^+)\right|^2}{\phi_{p'p'}(St)\phi_{u_i'u_i'}(St,\, y^+)} \left(\frac{u'_{rms}(y^+)}{U_0}\right)^2, \tag{4.11}$$

where $\phi_{p'p'}$ and $\phi_{u_i'u_i'}$ are the power spectral density of the pressure and velocity fluctuations, respectively. Here $\phi_{p'u_i'}$ denotes the cross-spectral density between them; u_1' and u_2' represent the tangential and normal velocity fluctuations, respectively; u'_{rms} is the root mean square of the tangential velocity fluctuation. Figure 15 presents the contribution of tangential velocity fluctuations to wall-pressure fluctuations. As shown in figure 15(*a*), the uncontrolled case exhibits a high-coherence region in the buffer layer ($5 \lesssim y^+ \lesssim 30$) across the investigated frequency range ($St = [0,20]$). This indicates a strong correlation between the tangential component of flow structures in this region and wall-pressure fluctuations, consistent with the experimental findings of Szőke *et al.* (2020*a*), which also report elevated coherence in the buffer layer. For cases X087A059 and X087A017, the location of the high-coherence region remains unchanged; however, both the extent and magnitude of coherence are reduced to varying degrees. In contrast, when suction is applied closer to the trailing edge, the coherence characteristics differ significantly. As shown in figure 15(*d*), a substantially enhanced high-coherence region emerges in the logarithmic region. This enhancement of low-frequency coherence may contribute to the reduced effectiveness of suction in case X093A059.

Unlike the distribution of $C_{p'u_1'}$, the contribution of normal fluctuations to wall-pressure fluctuations is primarily concentrated in the medium-to-high frequency range (see figure 16) (Pan & Ye 2025). For the uncontrolled case, the values of $C_{p'u_2'}$ are larger than those of $C_{p'u_1'}$ across the entire spectrum. This implies that the squeezing or lifting of vortex structures exerts a more significant impact on wall-pressure fluctuations. Additionally, the peak location of $C_{p'u_2'}$ also lies within the buffer layer. Suction control notably attenuates the contribution of normal vortex motion at the trailing edge to wall-pressure fluctuations, as depicted in figures 16(*b*) and 16(*c*). The coherence level in the optimal case X087A059 is relatively lower than that in X087A017. Undoubtedly, the attenuation of vortex-wall coherence facilitates noise reduction. Figure 16(*d*) reveals that while suction near the trailing edge attenuates the vortex-wall interactions within the buffer layer, it induces elevated coherence in both the viscous sublayer and logarithmic layer. Given the extensive spatial extent of the logarithmic region, the increased $C_{p'u_2'}$

https://doi.org/10.1017/jfm.2026.11154 Published online by Cambridge University Press

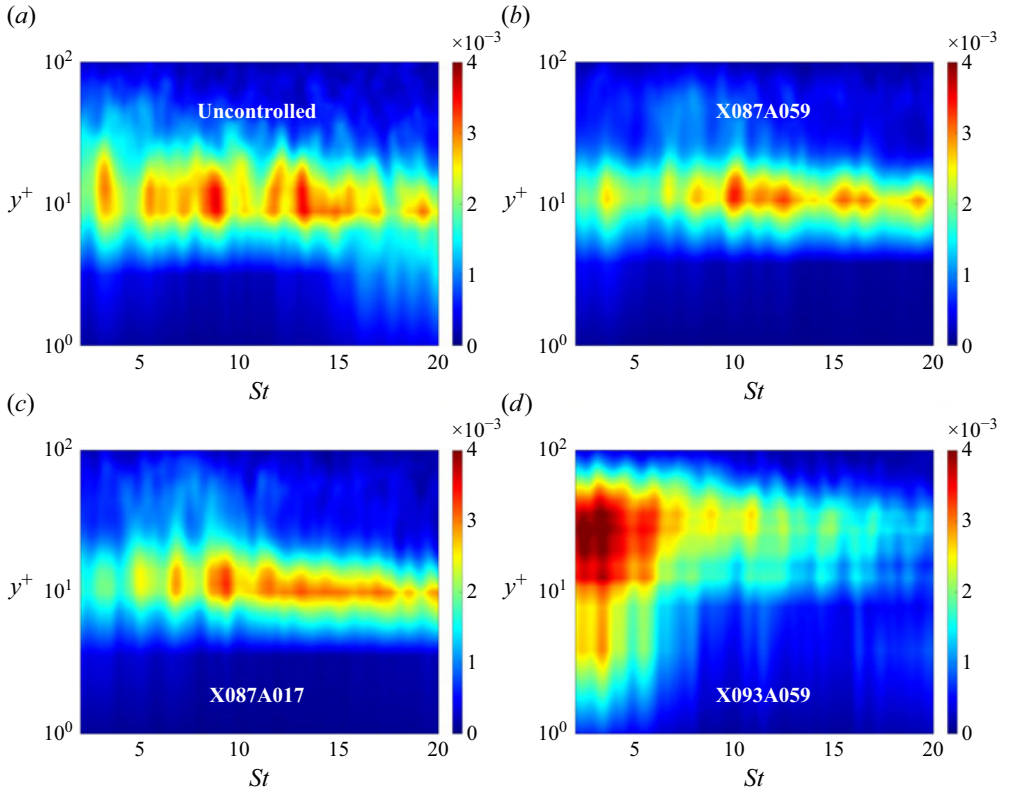


Figure 15. Pressure–velocity coherence $C_{p'u'_1}$ at $x/l_c = 0.96$: (*a*) the uncontrolled case, (*b*) the optimal case X087A059, (*c*) the suction case X087A017, and (*d*) the suction case X093A059.

magnitudes at mid-frequencies might impede noise reduction efforts. Moreover, in most regions of figures 15(*d*) and 16(*d*), the magnitude of $C_{p'u'_1}$ exceeds that of $C_{p'u'_2}$. This indicates that suction control in case X093A059 promotes the dominance of streamwise shear and convection of large-scale structures in governing wall-pressure fluctuations at the trailing edge.

To further elucidate why X087A059 achieves the optimal control effect, a quantitative comparison of the sound source intensity distributions near the trailing edge is conducted across different suction scenarios, as illustrated in figure 17. Suction markedly reduces the physical noise source intensity in the near field, with the optimal control case (X087A059) exhibiting the lowest $\sqrt{\langle\beta^2\rangle}$ values across all inner layers of the boundary layer. Notably, in the logarithmic region, X087A059 demonstrates a substantial reduction in physical sound source intensity compared with other suction cases. Additionally, the location of the peak sound source shifts. In the uncontrolled case, the maximum $\sqrt{\langle\beta^2\rangle}$ occurs at $y^+ \approx 20$, whereas for suction cases applied away from the trailing edge (X087A059 and X087A017), the peak shifts closer to the wall at $y^+ \approx 10$. It is noteworthy that the regions of high coherence in figures 15 and 16 coincide exactly with the buffer layer. However, when suction is applied near the trailing edge, the physical sound source intensity in the viscous sublayer is significantly amplified.

To gain a deeper understanding of the factors contributing to variations in sound source intensity, we utilise the trailing-edge scattering noise prediction model, known as the TNO model, developed by Parchen (1998). The TNO model comprises two components:

https://doi.org/10.1017/jfm.2026.11154 Published online by Cambridge University Press

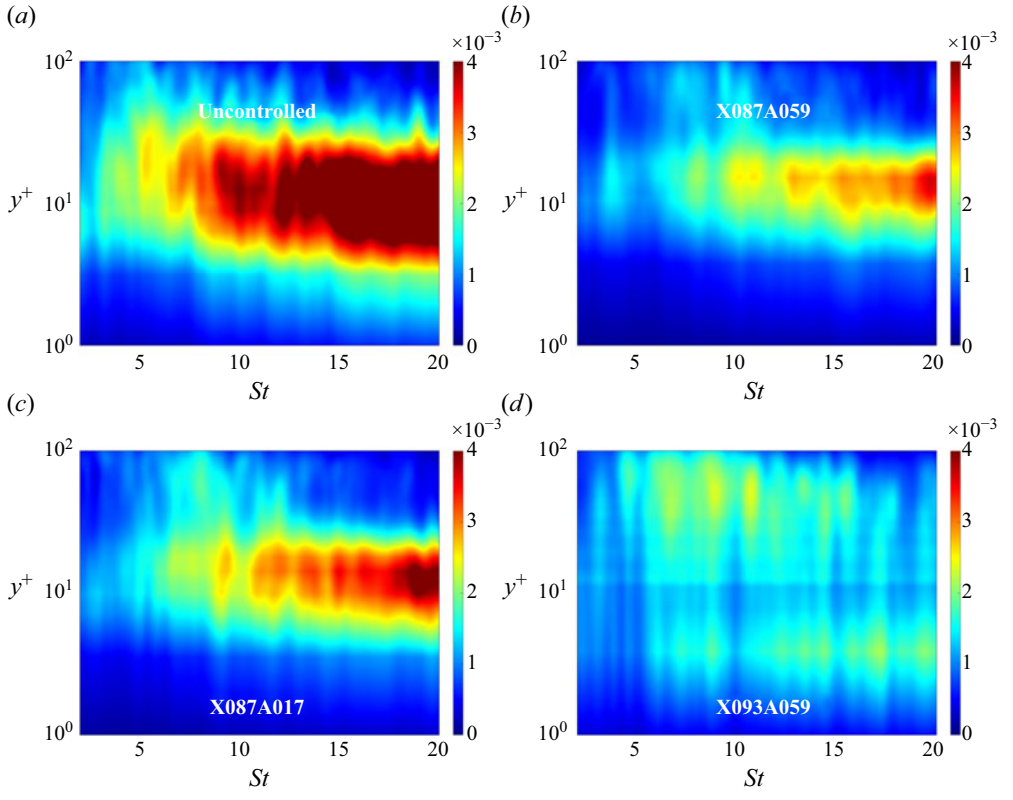


Figure 16. Pressure–velocity coherence $C_{p'u_2'}$ at $x/l_c = 0.96$: (*a*) the uncontrolled case, (*b*) the optimal case X087A059, (*c*) the suction case X087A017, and (*d*) the suction case X093A059.

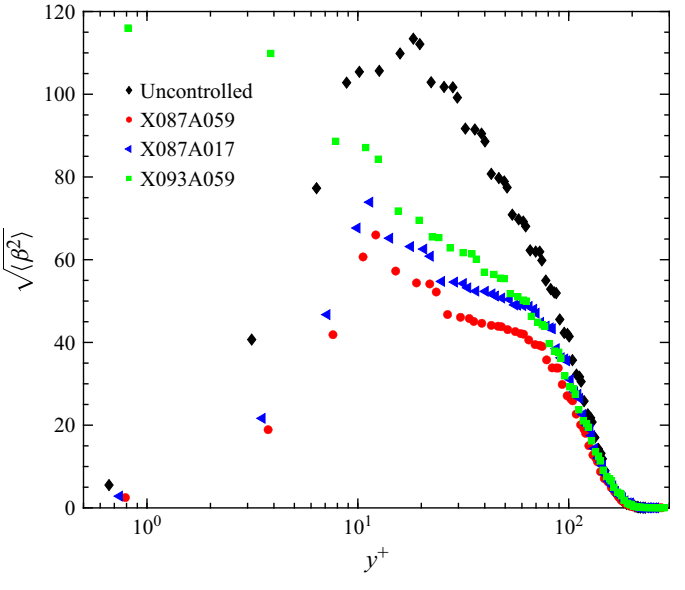


Figure 17. Profiles of the physical noise source intensity $\sqrt{\langle \beta^2 \rangle}$ as a function of dimensionless wall distance at $x/l_c = 0.96$.

https://doi.org/10.1017/jfm.2026.11154 Published online by Cambridge University Press

(i) the wavenumber–frequency wall-pressure spectrum derived by Blake (1986), and (ii) the prediction of far-field noise using trailing-edge diffraction theory (Howe 1978). For observer positions directly above the trailing edge, the TNO model's prediction can be expressed as (Kamruzzaman *et al.* 2011)

$$\Phi_{pp}(k_1, k_3, \omega) = 4\rho^2 \left(\frac{k_1^2}{k_1^2 + k_3^2}\right) \int_0^\infty \left[\frac{\partial U_1(y_2)}{\partial y_2}\right]^2 \Lambda_y(y_2)\langle u_2'^2(y_2)\rangle \cdot \widetilde{\phi}_{22}(k_1, k_3, y_2)\phi_m(\omega - k_1 U_c)e^{-2|k|y_2}\mathrm{d}y_2, \tag{4.12}$$

$$\mathrm{S}_{pp}(\omega) = \frac{\mathrm{L}}{4\pi \mathrm{R}^2} \int_{-\infty}^{\infty} \frac{\omega}{\mathrm{c}_0 k_1} \Phi_{pp}\,(k_1, 0, \omega)\,\mathrm{d}k_1, \tag{4.13}$$

where Φ_{pp} denotes the wavenumber–frequency spectrum of wall-pressure fluctuations and S_{pp} represents the far-field pressure power density spectrum. The variables k_1, k_3, ω, U_1 and y_2 denote the streamwise wavenumber, spanwise wavenumber, angular frequency, tangential velocity and wall-normal position, respectively. Here $k = \sqrt{k_1^2 + k_3^2}$. The parameters L and R denote the trailing-edge wetted length and the distance from the trailing edge to the observer, respectively. In the TNO model, the near-field sound source intensity is determined by the velocity gradient $\partial U_1(y_2)/\partial y_2$, vertical integral length scale $\Lambda_y(y_2)$ and mean square value of wall-normal velocity fluctuations $\langle u_2'^2(y_2)\rangle$. Under the frozen turbulence hypothesis, the moving-axis spectrum $\phi_m(\omega - k_1 U_c)$ can be reduced to a Dirac delta function. The normalised spectrum of vertical velocity fluctuations $\widetilde{\phi}_{22}$ (normalised by $\langle u_2'^2(y_2)\rangle$) determines the dominant source frequency, while the term $\mathrm{e}^{-2|k|y_2}$ tends to reduce the frequency of peak noise (Zhou *et al.* 2021). Thus, we can regard $(\partial U_1(y_2)/\partial y_2)^2 \Lambda_y(y_2)\langle u_2'^2(y_2)\rangle$ as a nominal source term in the TNO model (Wolf *et al.* 2015). Below, we analyse the effects of suction control on each component individually. Additionally, in some previous studies (Kamruzzaman *et al.* 2012), the calculation of the wall-pressure spectrum relied on isotropic modelling, which required the inclusion of an anisotropic correction factor (such as $f_{22}^{aniso} = \langle u_2'^2\rangle/2/3k_T$, where k_T represents the turbulent kinetic energy). However, in the current research, the TNO source term is obtained from large eddy simulations, so anisotropic correction is not considered. When evaluating far-field noise, the spectrum of wall-pressure fluctuations is typically measured near the trailing edge but at a sufficient distance to capture the incident pressure field of boundary layer turbulence (Sanjosé *et al.* 2019). Accounting for the suction slot position, we examine turbulence information at $x/l_c = 0.96$.

Figure 18(*a*) illustrates the modifications to the turbulent boundary layer velocity profile at the trailing edge induced by suction control. For suction control away from the trailing edge (X087A059 and X087A017), the influence on the viscous sublayer ($y^+ \lesssim 5$) is diminished, while the dimensionless velocity in the buffer layer ($5 \lesssim y^+ \lesssim 30$) exhibits a slight increase. In contrast, the effect of suction on the logarithmic region is most pronounced, with the velocity profile shifting towards the log-law. For the suction slot at $x/l_c \approx 0.87$, suction control with an angle of $\alpha \approx 0.59\pi$ induces more substantial modifications to the logarithmic region. Due to the closer proximity of the trailing edge to the suction slot, the boundary layer changes in X093A059 are more distinct, particularly in regions of $y^+ > 10$, where the dimensionless velocity shows a large decrease. However, in the TNO model, the velocity gradient plays an important role. Notably, while X093A059 exhibits the most significant velocity profile changes, its reduction in velocity gradient is less effective than that in X087A059. Figure 18(*b*) further presents the variation in velocity gradient within the logarithmic region induced by suction. Among all suction cases, the

https://doi.org/10.1017/jfm.2026.11154 Published online by Cambridge University Press

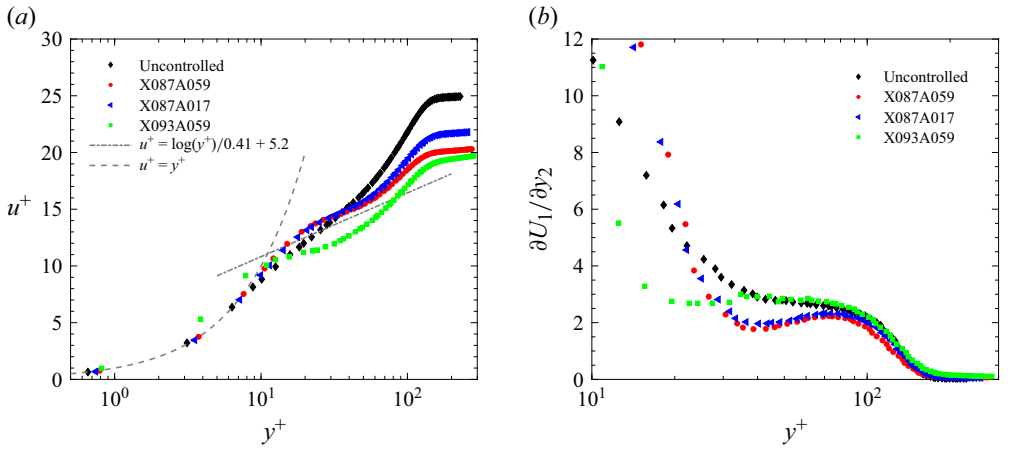


Figure 18. The turbulent boundary layer profiles at $x/l_c = 0.96$: (*a*) the dimensionless velocity profiles, and (*b*) the dimensionless velocity gradient profiles (non-dimensionalised by the speed of sound and aerofoil chord length).

optimal case X087A059 achieves the greatest reduction in velocity gradient within the region where $y^+ > 30$, while case X093A059 demonstrates greater efficacy in the buffer layer. Given the considerable extent of the log-law region, modifications to the velocity gradient in this zone contribute substantially to variations in the overall acoustic source strength.

Figure 19 presents the distribution of turbulent structure length scales at the trailing edge for different cases. The vertical integral length scale is calculated according to the Wilcox model (Wilcox 1998), namely,

$$\Lambda_y = \frac{1}{0.41}\sqrt{\frac{\left|\langle u_1' u_2' \rangle\right|}{(\partial U_1/\partial y_2)^2}}, \tag{4.14}$$

where u_1' and u_2' denote the velocity fluctuations tangential and normal to the wall, respectively. The spanwise length scale Λ_z is obtained directly by integrating the autocorrelation function of the spanwise velocity fluctuations. As can be seen in figure 19(*a*), the vertical integral length scales generally increase for both case X087A059 and case X087A017, except for a few specific locations. In contrast, case X093A059 exhibits increased vertical integral length scales only in the near-wall region, with significant reductions observed where $y_2/\delta_0 > 0.2$. The behaviour of the spanwise integrated length scales, however, exhibits distinct behaviour, as illustrated in figure 19(*b*). In the near-wall region, Λ_z exhibits an increase, whereas in regions farther from the wall ($y_2/\delta_0 > 0.2$), these scales decrease to varying degrees across all suction cases, with case X087A059 showing the most pronounced reduction. In the TNO model, only the vertical integral length scales influence wall-pressure fluctuations. The results in figure 19(*a*) suggest that variations in length scales are not the primary driver of noise reduction, a finding consistent with the experiments by Wolf *et al.* (2015).

Within the nominal acoustic source term of the TNO model, the wall-normal Reynolds stress component also plays a critical role. As shown in figure 20, suction induces varying degrees of reduction in the wall-normal Reynolds stress component across different boundary layer regions. Notably, substantial attenuation occurs within the log-law region. Furthermore, case X087A059 exhibits the weakest wall-normal velocity fluctuations throughout the boundary layer, a key factor contributing to its maximum noise reduction.

https://doi.org/10.1017/jfm.2026.11154 Published online by Cambridge University Press

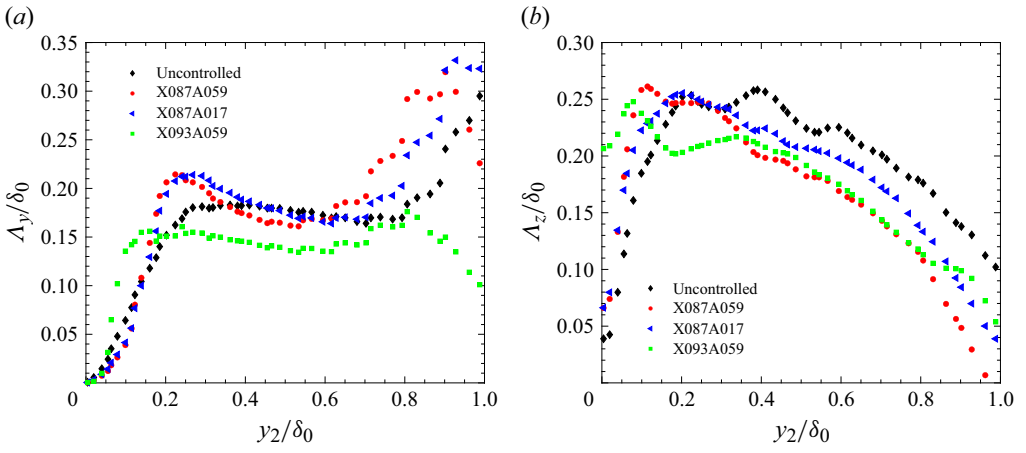


Figure 19. Length scales of turbulent structures at $x/l_c = 0.96$: (*a*) the vertical integral length scale Λ_y, and (*b*) the spanwise integrated length scale Λ_z, where δ_0 represents the boundary layer thickness at the trailing edge for the uncontrolled case.

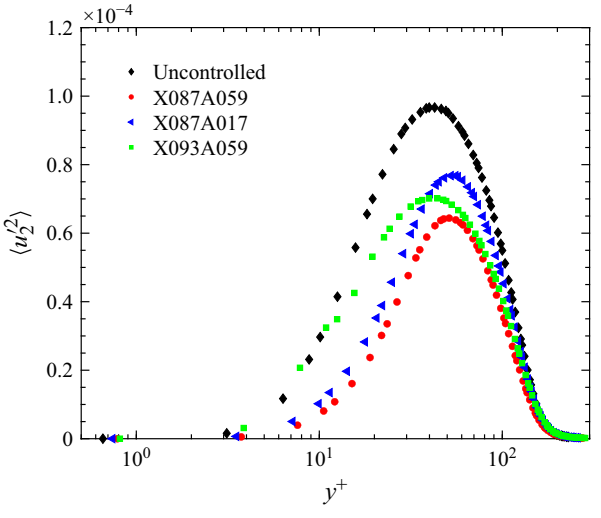


Figure 20. Profiles of the Reynolds stress component in the wall-normal direction $\langle u_2'^2 \rangle$ as a function of dimensionless wall distance at $x/l_c = 0.96$.

Additionally, certain suction controls shift the peak location of the wall-normal Reynolds stress component. In the uncontrolled case, the peak resides at $y^+ \approx 40$. For cases X087A059 and X087A017, the peak location shifts away from the wall to $y^+ \approx 50$; while case X093A059 shows negligible displacement, maintaining its peak position.

The total nominal source term of the TNO model $(\partial U_1/\partial y_2)^2 \Lambda_y \langle u_2'^2 \rangle$ is examined in figure 21. In the uncontrolled case, the peak of the TNO source term resides at $y^+ \approx 20$, closely aligned with the peak location of the physical acoustic source strength $\sqrt{\langle \beta^2 \rangle}$ shown in figure 17. In suction-controlled cases the magnitude of the TNO source term is markedly reduced. The most substantial attenuation occurs in the logarithmic region, particularly in the optimal noise reduction case (X087A059). Given the extensive spatial extent of the logarithmic region, the source term in this region significantly contributes

https://doi.org/10.1017/jfm.2026.11154 Published online by Cambridge University Press

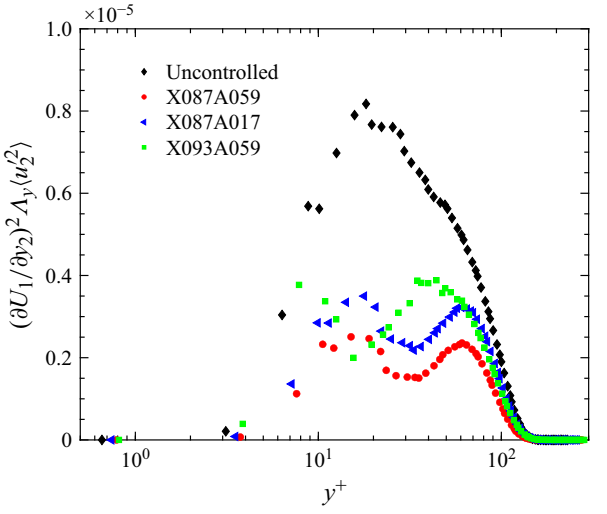


Figure 21. Profiles of $(\partial U_1/\partial y_2)^2 \Lambda_y \langle u_2'^2 \rangle$ as a function of dimensionless wall distance at $x/l_c = 0.96$.

to the overall radiated noise. Additionally, the source term in suction cases exhibits a dual-peak structure. The peak locations for cases X087A059 and X087A017 are closely aligned but shifted farther from the wall compared with case X093A059. The generation of the dual-peak structure results from the combined effects of changes in boundary layer velocity gradients, wall-normal Reynolds stresses and variations in the vertical integral length scale. This suggests that suction control may have altered the primary region of noise generation – shifting it from being dominated by the buffer layer to a joint dominance by both the buffer layer and the logarithmic layer. A comparison of figures 17 and 21 reveals that, despite differences in the distributions of the physical noise source and the TNO source term in suction cases, both consistently highlight the critical role of source attenuation in the logarithmic region for achieving optimal noise reduction in case X087A059. From an engineering perspective, a suction control device placed at a distance from the trailing edge and slightly angled towards the upstream direction can more effectively reduce the source strength and lower the far-field noise.

In short, case X087A059 dramatically suppresses pressure–velocity coherence within the boundary layer, thereby facilitating noise reduction, whereas the suction near the trailing edge (X093A059) amplifies the footprint of logarithmic layer turbulence in wall-pressure fluctuations. Moreover, case X087A059 achieves optimal noise reduction primarily by substantially diminishing the velocity gradient at the trailing edge and suppressing wall-normal Reynolds stress components, thereby inducing a marked decrease in sound source intensity within the logarithmic region. The alterations in turbulence length scales do not play decisive roles in the noise attenuation mechanism.

5. Summary and conclusions

In this study, ILES are conducted on a NACA0012 aerofoil with and without trailing-edge blowing/suction. The results are obtained under constant flow control intensity ($C_\mu = 0.8$) and fixed control slot length ($b = 0.05 l_c$). The centre position and angle of the active control region are described as optimisation variables, with respective value ranges of $[0.825 l_c, 0.975 l_c]$ and $[0, 2\pi]$. To achieve maximum noise reduction, two rounds of optimisation are applied: direct Bayesian optimisation and sound-source-oriented

https://doi.org/10.1017/jfm.2026.11154 Published online by Cambridge University Press

coarse-grained optimisation. Some typical cases are examined to elucidate changes in far-field noise and near-field turbulence structures, while the underlying noise reduction mechanisms under optimal control settings are investigated.

In the direct Bayesian optimisation process, the mean overall SPL ($\overline{\Delta\mathrm{OASPL}}$) in the far field is selected as the objective function, while the parallel upper confidence bound (q-UCB) policy is employed as the acquisition function. Each optimisation iteration requires the execution of five high-fidelity 3D simulations. For the first round of Bayesian optimisation, 15 iterations are conducted, with the optimal noise reduction parameters obtained at the fifth iteration. The final optimal parameters include a suction location at $x/l_c = 0.8734$ and an angle of $\alpha/\pi = 0.5895$, resulting in a reduction of $\overline{\Delta\mathrm{OASPL}}$ by up to 3.7 dB.

To reduce the computational cost of direct Bayesian optimisation, the surrogate model is constructed based on the physical noise source defined by the multi-process acoustic theory. This approach works because statistically processing physical sound sources offers low signal latency and quick convergence, which dramatically reduces the cost of the optimisation workflow. It should emphasise that the GP models constructed by noise reduction and physical source intensity demonstrate similar landscapes. Specifically, all blowing control amplifies both sound source intensity and noise levels. Suction adjacent to the trailing edge exhibits poor noise reduction efficacy. As the suction slot shifts upstream, effective control angles expand progressively from wall-normal suction toward broader orientations. The optimal control parameters obtained by both GP models are similar. The GP model demonstrates the feasibility of sound-source-oriented coarse-grained Bayesian optimisation, even though its physical source cannot capture multiple extrema in the noise reduction landscape. Subsequently, we implement this source-oriented Bayesian optimisation, achieving comparable noise reduction within merely two iterations. Under the current statistical strategy, the source-oriented Bayesian optimisation reduces the cost per sampling by 60 %. Considering the reduction in required iterations, the source-oriented optimisation can reduce the total computational cost to approximately one-sixth of the initial direct optimisation.

Next, the changes in noise and flow structures under blowing or suction control are examined through several typical cases. The blowing control generates additional large-scale vortex shedding, which significantly enhances noise radiation within the low-frequency range ($St = [2, 6]$). In the most energetic DMD mode of the blowing case (X087A150), an antisymmetric structure associated with this vortex shedding is observed. Furthermore, the suction control does not shift the dominant frequency band of the DMD modes ($St = [5, 6]$), but it substantially reduces the mode energy across all frequencies. Among these suction cases, X087A059 demonstrates the most pronounced effect, effectively disrupting the coherent mode structures in the near field and thereby achieving the greatest reduction in both mode energy and radiated noise. The anisotropic invariant map indicates that the suction control has a significant impact on the near-wall turbulent structures, with case X087A059 exhibiting the most substantial alterations in the logarithmic layer.

Finally, pressure–velocity coherence analysis reveals that the optimal suction control (X087A059) substantially reduces pressure–velocity coherence within the boundary layer, contributing to effective noise reduction. In contrast, suction near the trailing edge (X093A059) significantly amplifies the footprint of logarithmic layer turbulent motions within surface pressure fluctuations, potentially explaining its suboptimal acoustic performance. Quantitative analysis of physical noise sources reveals that case X087A059 exhibits the weakest sound source intensity in the logarithmic layer, which can be regarded

https://doi.org/10.1017/jfm.2026.11154 Published online by Cambridge University Press

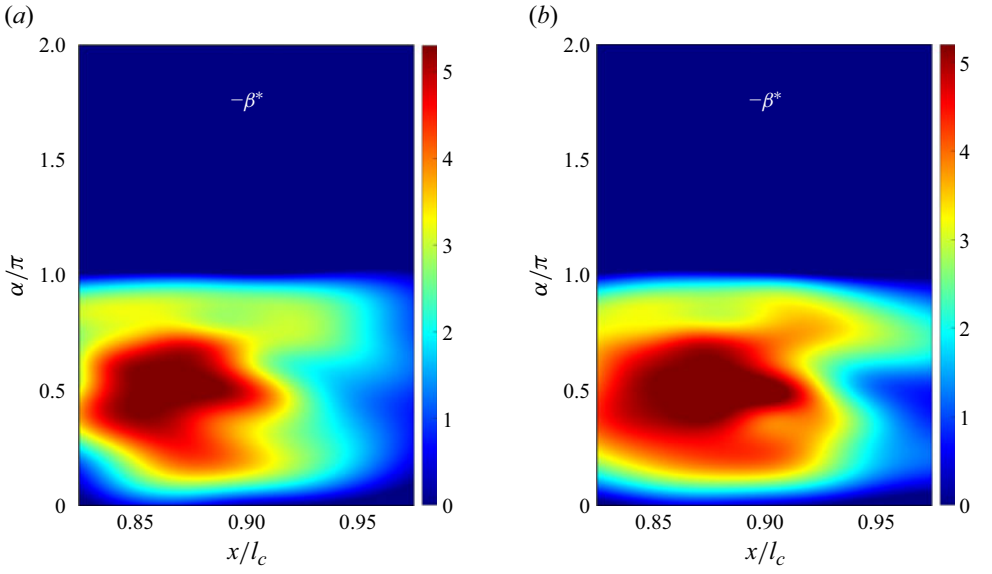


Figure 22. The GP models based on near-field physical noise source strength $-\beta^*$: (*a*) the integration volume $V \in [l_c - 2\delta_0, l_c + \delta_0] \times [-1.5\delta_0, 1.5\delta_0] \times [0, 0.1l_c]$; (*b*) the integration volume $V \in [l_c - \delta_0, l_c + 0.5\delta_0] \times [-\delta_0, \delta_0] \times [0, 0.1l_c]$.

as the primary factor contributing to its optimal noise reduction performance. Using the TNO model, it is found that the decrease in logarithmic layer velocity gradients and diminishing wall-normal Reynolds stresses dominate the attenuation of noise source strength, while changes in turbulent length scales have minimal impact.

In reality, this work introduces a novel framework that integrates Bayesian optimisation with advanced noise diagnostic theory. This framework effectively achieved active control to mitigate TBL-TE noise at a significantly reduced cost. The elucidated noise reduction mechanism offers valuable insights for future TBL-TE noise control strategies. Furthermore, this study suggests that a source-informed, multi-fidelity Bayesian optimisation framework could also be utilised to address multi-objective design challenges in aerodynamics and aeroacoustics in the future.

Acknowledgements. The numerical computations in this paper have been performed at Hefei Advanced Computing Center.

Funding. This work is supported by the National Natural Science Foundation of China under grant Nos. 12388101, 12322210, 12402317, 92252202, and 12172351, the Strategic Priority Research Program of the Chinese Academy of Sciences (Grant No. XDB0500301) and the Fundamental Research Funds for the Central Universities.

Declaration of interests. The authors report no conflict of interest.

Data availability statement. The data that support the findings of this study are available from the corresponding author upon reasonable request.

Appendix. Selection of the sound source integration domain

To illustrate the impact of integration volume selection on β^*, we compared the GP model from figure 6 with another model based on a smaller integration volume. It can be observed that altering the integration domain only slightly affects the predicted distribution of β^*

https://doi.org/10.1017/jfm.2026.11154 Published online by Cambridge University Press

(see figure 22). The noise reduction trends and the identified optimal parameter regions obtained from different integration domains are generally consistent. Additionally, it should be noted that the objective of the present optimisation framework is to indicate the region where the optimal control parameters are located. This can be achieved as long as our integration volume covers the primary variation region of the sound source. For more precise noise reduction capture, a multi-fidelity Bayesian approach should be employed.

References

Antonia, R., Zhu, Y. & Sokolov, M. 1995 Effect of concentrated wall suction on a turbulent boundary layer. *Phys. Fluids* **7** (10), 2465–2474.

Arnold, B., Lutz, T., Krämer, E. & Rautmann, C. 2018 Wind-turbine trailing-edge noise reduction by means of boundary-layer suction. *AIAA J.* **56** (5), 1843–1854.

Avallone, F., Van Der Velden, W.C.P., Ragni, D. & Casalino, D. 2018 Noise reduction mechanisms of sawtooth and combed-sawtooth trailing-edge serrations. *J. Fluid Mech.* **848**, 560–591.

Ayton, L.J. 2018 Analytic solution for aerodynamic noise generated by plates with spanwise-varying trailing edges. *J. Fluid Mech.* **849**, 448–466.

Blake, W.K. 1986 *Mechanics of Flow-Induced Sound and Vibration*, vol. I and II. Academic press.

Blanchard, A.B., Cornejo Maceda, GY., Fan, D.-W., Li, Y.-Q., Zhou, Y., Noack, B.R. & Sapsis, T.P. 2021 Bayesian optimization for active flow control. *Acta Mechanica Sin.* **37** (12), 1786–1798.

Brooks, T.F., Pope, D. & Marcolini, M.A. 1989 Airfoil self-noise and prediction. *Tech. Rep*. 1218.

Carpio, A.R., Martínez, R.M., Avallone, F., Ragni, D., Snellen, M. & van der Zwaag, S. 2019 Experimental characterization of the turbulent boundary layer over a porous trailing edge for noise abatement. *J. Sound Vib.* **443**, 537–558.

Cesar, L.M., Kamliya Jawahar, H. & Azarpeyvand, M. 2018 Airfoil trailing-edge noise reduction using flow suction. In *2018 AIAA/CEAS Aeroacoustics Conference, Atlanta, GA, USA*, *AIAA Paper* 2018-2814. American Institute of Aeronautics and Astronautics.

Chaitanya, P. & Vellanki, P. 2021 Bayesian optimisation for low-noise aerofoil design with aerodynamic constraints. *Intl J. Aeroacoust.* **20** (1–2), 109–129.

Chong, T.P. & Vathylakis, A. 2015 On the aeroacoustic and flow structures developed on a flat plate with a serrated sawtooth trailing edge. *J. Sound Vib.* **354**, 65–90.

Clark, I.A., Alexander, W.N., Devenport, W.J., Glegg, S.A.L., Jaworski, J.W., Daly, C.A. & Peake, N. 2017 Bioinspired trailing-edge noise control. *AIAA J.* **55** (3), 740–754.

Doolan, C. & Moreau, D. 2022 *Flow Noise: Theory*. Springer Nature.

Fahland, G., Stroh, A., Frohnapfel, B., Atzori, M., Vinuesa, R., Schlatter, P. & Gatti, D. 2021 Investigation of blowing and suction for turbulent flow control on airfoils. *AIAA J.* **59** (11), 4422–4436.

Fukagata, K., Iwamoto, K. & Kasagi, N. 2002 Contribution of Reynolds stress distribution to the skin friction in wall-bounded flows. *Phys. Fluids* **14** (11), L73–L76.

Gstrein, F., Zang, B. & Azarpeyvand, M. 2023 Trailing-edge noise reduction through finlet-induced turbulence. *J. Fluid Mech.* **959**, A24.

Guo, J., Maryami, R., Yang, C.-H., Yang, Y.-N., Wang, X.-N. & Liu, Y. 2023 Aerodynamic noise reduction of a blunt flat plate by trailing-edge blowing. *Phys. Fluids* **35** (6), 065116.

Han, B.-Z., Huang, W.-X. & Xu, C.-X. 2023 Multi-fidelity Bayesian optimization for spatially distributed control of flow over a circular cylinder. *Phys. Fluids* **35** (11), 115144.

Herr, M. & Reichenberger, J. 2011 In search of airworthy trailing-edge noise reduction means. In *17th AIAA/CEAS Aeroacoustics Conference (32nd AIAA Aeroacoustics Conference), Portland, OR, USA*, *AIAA Paper* 20177-2780. American Institute of Aeronautics and Astronautics.

Howe, M.S. 1978 A review of the theory of trailing edge noise. *J. Sound Vib.* **61** (3), 437–465.

Hu, Y.-S., Wan, Z.-H., Ye, C.-C., Sun, D.-J. & Lu, X.-Y. 2022 Noise reduction mechanisms for insert-type serrations of the NACA-0012 airfoil. *J. Fluid Mech.* **941**, A57.

Huang, X. 2017 Theoretical model of acoustic scattering from a flat plate with serrations. *J. Fluid Mech.* **819**, 228–257.

Jaworski, J.W. & Peake, N. 2013 Aerodynamic noise from a poroelastic edge with implications for the silent flight of owls. *J. Fluid Mech.* **723**, 456–479.

Jenkins, W.F., Gerstoft, P. & Park, Y. 2023 Bayesian optimization with Gaussian process surrogate model for source localization. *J. Acoust. Soc. Am.* **154** (3), 1459–1470.

Jones, L.E. & Sandberg, R.D. 2012 Acoustic and hydrodynamic analysis of the flow around an aerofoil with trailing-edge serrations. *J. Fluid Mech.* **706**, 295–322.

https://doi.org/10.1017/jfm.2026.11154 Published online by Cambridge University Press

KAMETANI, Y. & FUKAGATA, K. 2011 Direct numerical simulation of spatially developing turbulent boundary layers with uniform blowing or suction. *J. Fluid Mech.* **681**, 154–172.

KAMETANI, Y., FUKAGATA, K., ÖRLÜ, R. & SCHLATTER, P. 2015 Effect of uniform blowing/suction in a turbulent boundary layer at moderate Reynolds number. *Intl J. Heat Fluid Flow* **55**, 132–142.

KAMRUZZAMAN, M., HERRIG, A., LUTZ, T., WÜRZ, W., KRÄMER, E. & WAGNER, S. 2011 Comprehensive evaluation and assessment of trailing edge noise prediction based on dedicated measurements. *Noise Control Engng J.* **59** (1), 54–67.

KAMRUZZAMAN, M., LUTZ, TH, HERRIG, A. & KRÄMER, E. 2012 Semi-empirical modeling of turbulent anisotropy for airfoil self-noise predictions. *AIAA J.* **50** (1), 46–60.

KISIL, A. & AYTON, L.J. 2018 Aerodynamic noise from rigid trailing edges with finite porous extensions. *J. Fluid Mech.* **836**, 117–144.

KORNILOV, V., KAVUN, I. & POPKOV, A. 2021 Technology of combined turbulent flow control on an airfoil by distributed air blowing/suction. *AIP Conf. Proc.* **2351** (1), 020001.

KUMAR, S. & BHUMKAR, Y.G. 2024 Modification in airfoil's tonal noise using periodic suction-blowing excitation. *J. Sound Vib.* **587**, 118495.

LEE, H. & KANG, S.-H. 2000 Flow characteristics of transitional boundary layers on an airfoil in wakes. *J. Fluids Engng* **122** (3), 522–532.

LEE, S., AYTON, L.J., BERTAGNOLIO, F., MOREAU, S., CHONG, T.P. & JOSEPH, P. 2021 Turbulent boundary layer trailing-edge noise: theory, computation, experiment, and application. *Prog. Aerosp. Sci.* **126**, 100737.

LI, J.-C. & ZHANG, M.-Q. 2022 Reinforcement-learning-based control of confined cylinder wakes with stability analyses. *J. Fluid Mech.* **932**, A44.

LI, Y.-Q., NOACK, B.R., WANG, T.-Y., CORNEJO MACEDA, GY., PICKERING, E., SHAQARIN, T. & TYLISZCZAK, A. 2024 Jet mixing enhancement with Bayesian optimization, deep learning and persistent data topology. *J. Fluid Mech.* **991**, A5.

LIANG, L.-L., WAN, Z.-H., SHE, M.-X., ZHANG, P.-J.-Y., SUN, D.-J. & LU, X.-Y. 2024 Active noise control of a supersonic underexpanded planar jet guided by resolvent analysis. *J. Fluid Mech.* **1001**, A11.

LIM, S., GARBO, A., BEKEMEYER, P., APPEL, C., EWERT, R. & DELFS, J. 2022 High-fidelity aerodynamic and aeroacoustic multi-objective Bayesian optimization. In *Proceedings of the AIAA Aviation 2022 Forum, Chicago, IL, USA*, 27 June–1 July 2022, p. 3354. American Institute of Aeronautics and Astronautics.

LUMLEY, J.L. & NEWMAN, G.R. 1977 The return to isotropy of homogeneous turbulence. *J. Fluid Mech.* **82** (1), 161–178.

LYU, B.-S., AZARPEYVAND, M. & SINAYOKO, S. 2016 Prediction of noise from serrated trailing edges. *J. Fluid Mech.* **793**, 556–588.

MAHFOZE, O.A., MOODY, A., WYNN, A., WHALLEY, R.D. & LAIZET, S. 2019 Reducing the skin-friction drag of a turbulent boundary-layer flow with low-amplitude wall-normal blowing within a Bayesian optimization framework. *Phys. Rev. Fluids* **4** (9), 094601.

MANEGAR, F.A., STAHL, K., CAROLUS, T.H. & BINOIS, R. 2019 Noise reduction mechanism of trailing edge blowing using the lattice-Boltzmann method: numerical and experimental analysis. In *Inter-noise and noise-con congress and conference proceedings*, vol. 259, pp. 3818–3828. Institute of Noise Control Engineering.

MAO, F., KANG, L.-L., WU, J.-Z., YU, J.-L., GAO, A.-K., SU, W.-D. & LU, X.-Y. 2020 A study of longitudinal processes and interactions in compressible viscous flows. *J. Fluid Mech.* **893**, A23.

MATÉRN, B. 2013 *Spatial Variation*, vol. 36. Springer Science & Business Media.

MOREAU, S., LAFFAY, P., IDIER, A. & ATALLA, N. 2016 Several noise control of the trailing-edge noise of a controlled-diffusion airfoil. In *22nd AIAA/CEAS Aeroacoustics Conference, Lyon, France*, *AIAA Paper* 2016-2816. American Institute of Aeronautics and Astronautics.

NAJAFI-YAZDI, A., BRÈS, G.A. & MONGEAU, L. 2011 An acoustic analogy formulation for moving sources in uniformly moving media. *Proc. R. Soc. Lond. A* **467** (2125), 144–165.

OYEWOLA, O., DJENIDI, L. & ANTONIA, R. 2003 Combined influence of the Reynolds number and localised wall suction on a turbulent boundary layer. *Exp. Fluids* **35**, 199–206.

PAN, Z.-H. & YE, Q.-Q. 2025 Manipulation of mid-and high-frequency wall-pressure sources by streamwise finlets. *J. Fluid Mech.* **1005**, A8.

PARCHEN, R. 1998 *Progress Report DRAW: A Prediction Scheme for Trailing Edge Noise Based on Detailed Boundary Layer Characteristics*. TNO Institute of Applied Physics.

PARK, J. & CHOI, H. 1999 Effects of uniform blowing or suction from a spanwise slot on a turbulent boundary layer flow. *Phys. Fluids* **11** (10), 3095–3105.

PEREIRA, L.T.L., AVALLONE, F., RAGNI, D. & SCARANO, F. 2022 A physics-based description and modelling of the wall-pressure fluctuations on a serrated trailing edge. *J. Fluid Mech.* **938**, A28.

PERSHIN, A., BEAUME, C., EAVES, T.S. & TOBIAS, S.M. 2022 Optimizing the control of transition to turbulence using a Bayesian method. *J. Fluid Mech.* **941**, A25.

https://doi.org/10.1017/jfm.2026.11154 Published online by Cambridge University Press

POPE, S.B. 2001 Turbulent flows. *Meas. Sci. Technol.* **12** (11), 2020–2021.
QUADRIO, M., CHIARINI, A., BANCHETTI, J., GATTI, D., MEMMOLO, A. & PIROZZOLI, S. 2022 Drag reduction on a transonic airfoil. *J. Fluid Mech.* **942**, R2.
REUMSCHÜSSEL, J.M., LI, Y.-Q., ZUR NEDDEN, P.M., WANG, T.-Y., NOACK, B.R. & PASCHEREIT, C.O. 2024 Experimental jet control with Bayesian optimization and persistent data topology. *Phys. Fluids* **36** (9), 095164.
SANJOSÉ, M., MOREAU, S., LYU, B.-S. & AYTON, L.J. 2019 Analytical, numerical and experimental investigation of trailing-edge noise reduction on a Controlled Diffusion airfoil with serrations. In *20th AIAA/CEAS Aeroacoustics Conference, Atlanta, GA, USA*, *AIAA Paper* 2014-2324. American Institute of Aeronautics and Astronautics.
SCHMID, P.J. 2010 Dynamic mode decomposition of numerical and experimental data. *J. Fluid Mech.* **656**, 5–28.
SCHULZE, J. & SESTERHENN, J. 2013 Optimal distribution of porous media to reduce trailing edge noise. *Comput. Fluids* **78**, 41–53.
SHAHRIARI, B., SWERSKY, K., WANG, Z.-Y., ADAMS, R.P. & DE FREITAS, N. 2015 Taking the human out of the loop: a review of Bayesian optimization. *Proc. IEEE* **104** (1), 148–175.
SIMONSEN, A. & KROGSTAD, P.-Å. 2005 Turbulent stress invariant analysis: clarification of existing terminology. *Phys. Fluids* **17** (8), 088103.
STEIN, M.L. 1999 *Interpolation of Spatial Data: Some Theory for Kriging*. Springer Science & Business Media.
SZŐKE, M., FISCALETTI, D. & AZARPEYVAND, M. 2018 Effect of inclined transverse jets on trailing-edge noise generation. *Phys. Fluids* **30** (8), 085110.
SZŐKE, M., FISCALETTI, D. & AZARPEYVAND, M. 2020*a* Influence of boundary layer flow suction on trailing edge noise generation. *J. Sound Vib.* **475**, 115276.
SZŐKE, M., FISCALETTI, D. & AZARPEYVAND, M. 2020*b* Uniform flow injection into a turbulent boundary layer for trailing edge noise reduction. *Phys. Fluids* **32** (8), 085104.
TERUNA, C., MANEGAR, F., AVALLONE, F., RAGNI, D., CASALINO, D. & CAROLUS, T. 2020 Noise reduction mechanisms of an open-cell metal-foam trailing edge. *J. Fluid Mech.* **898**, A18.
WILCOX, D.C. 1998 *Turbulence Modeling for CFD*, vol. 2. DCW industries.
WILSON, J.T., MORICONI, R., HUTTER, F. & DEISENROTH, M.P. 2017 The reparameterization trick for acquisition functions. arXiv preprint arXiv:1712.00424.
WITHERDEN, F.D., FARRINGTON, A.M. & VINCENT, P.E. 2014 PyFR: an open source framework for solving advection–diffusion type problems on streaming architectures using the flux reconstruction approach. *Comput. Phys. Commun.* **185** (11), 3028–3040.
WOLF, A., LUTZ, T., WÜRZ, W., KRÄMER, E., STALNOV, O. & SEIFERT, A. 2015 Trailing edge noise reduction of wind turbine blades by active flow control. *Wind Energy* **18** (5), 909–923.
XU, K.-W. & ZHA, G.-C. 2020 Investigation of coflow jet active flow control for wind turbine airfoil. In *AIAA Aviation 2020 Forum, Reston, VA, USA*, p. 2942. American Institute of Aeronautics and Astronautics.
YANG, C.-H., ARCONDOULIS, E.J., YANG, Y.-N., GUO, J., MARYAMI, R., BI, C.-X. & LIU, Y. 2023 Active control of airfoil turbulent boundary layer noise with trailing-edge blowing. *J. Acoust. Soc. Am.* **153** (4), 2115–2115.
YANG, C.-H., LIU, Y., ZHANG, X.-Z. & BI, C.-X. 2024 Hybrid control of aerofoil self-noise by coupling air blowing and trailing-edge serration. *J. Sound Vib.* **575**, 118265.
YU, F.-Y., WAN, Z.-H., HU, Y.-S., SUN, D.-J. & LU, X.-Y. 2025 Effects of leading-edge serration shape on noise reduction in rod-airfoil interactions. *J. Acoust. Soc. Am.* **157** (1), 215–233.
ZANG, B., MAYER, Y.D. & AZARPEYVAND, M. 2020 A note on the pressure–velocity correlation and coherence normalisation. *Exp. Fluids* **61** (8), 186.
ZHA, G.-C., REN, Y., GAN, J.-Y. & ESPINAL, D. 2019 A high efficiency low noise VTOL/ESTOL concept using coflow jet airfoil. In *2019 AIAA/IEEE Electric Aircraft Technologies Symposium (EATS)*, pp. 1–25. IEEE.
ZHOU, P., ZHONG, S.-Y. & ZHANG, X. 2021 On the effect of velvet structures on trailing edge noise: experimental investigation and theoretical analysis. *J. Fluid Mech.* **919**, A11.
ZIGUNOV, F., SELLAPPAN, P. & ALVI, F.S. 2022 Reduction of noise in cold and hot supersonic jets using active flow control guided by a genetic algorithm. *J. Fluid Mech.* **952**, A40.

https://doi.org/10.1017/jfm.2026.11154 Published online by Cambridge University Press